Nanocrystalline tungsten at high radiation exposure

Pui-Wai Ma,[*] Daniel R. Mason,[†] Steven Van Boxel,[‡] and Sergei L. Dudarev[§]
United Kingdom Atomic Energy Authority, Culham Science Centre, Abingdon, Oxfordshire OX14 3DB, United Kingdom

(Received 14 August 2023; revised 27 April 2024; accepted 11 June 2024; published 1 August 2024)

Evolution of nanocrystalline (NC) tungsten under radiation exposure is investigated by atomic scale simulations in the low temperature high dose limit. Statistical analysis of samples containing at least a million atoms, with grain size varying from 5 nm to 20 nm, shows that the pattern of microstructural evolution of a NC material differs significantly from that of a single crystal. The high resistance to swelling in the low grain size limit stems from a combined effect of the initial excess volume of atomic configurations at grain boundaries and high integral volume of grain boundary defect-denuded zones. Grain boundaries annihilate defects through the rearrangement of their local atomic configurations acting as fluctuating dynamic sinks for defects. Grain size distribution slowly broadens as a function of dose, delaying the onset of an asymptotic radiation-driven steady state in comparison with a single crystalline material. Spatial limitations imposed by the size and topology of grains prevent the formation of a percolating dislocation network, resulting in only isolated dislocation loops being retained in the microstructure even at high radiation exposure.

DOI: 10.1103/PhysRevMaterials.8.083601

I. INTRODUCTION

Tungsten has been selected as a candidate material for plasma facing components of fusion devices due to its unique combination of high melting temperature, good thermal conductivity, and low thermal expansion [1,2]. Tungsten also has a low physical sputtering yield [3] and favorable radioactive decay sequence for the isotopes produced by neutron transmutations [4], compatible with low-activation requirements.

A burning fusion plasma produces helium and high-energy neutrons from fusion reactions between deuterium and tritium nuclei. The high energy neutrons propagate into the materials to the depth of tens of centimeters [5], undergoing elastic and inelastic interactions with atomic nuclei and generating γ photons [6] and atomic recoils [7]. These recoils initiate collision cascades, producing microscopic structural defects from where complex microstructural features, including dense vacancy atmospheres, phase inclusions, and dislocation networks, emerge in the limit of high dose [7–15]. Lattice defects, such as Frenkel pairs, dislocations, dislocation loops, and voids, degrade the thermal [16–18] and mechanical [19,20] properties of tungsten, limiting its lifetime in a fusion reactor environment.

Neutron irradiation-induced swelling [21,22] and dimensional changes [23] are phenomena critical to the structural integrity of components in fission and fusion power plants [24]. From the experimental perspective, void formation is a signature manifestation of swelling [25], where the fundamental cause of volumetric expansion is the growth of a dislocation network by the coalescence of self-interstitial atom defect clusters [11,14,26]. Voids form in neutron irradiated tungsten at elevated temperatures [19,21] and the high concentration of vacancies and nanometer-size vacancy clusters, invisible in transmission electron microscope (TEM) images [8,27,28], is confirmed by positron annihilation spectroscopy [29,30].

Materials with complex microstructure exhibit greater stability under irradiation. Ferritic-martensitic steels show significantly improved resistance to neutron-irradiation-induced swelling in comparison with pure alloys with similar chemical composition [22,31,32]. Some high entropy alloys [33,34] also exhibit lower swelling under ion irradiation. Nanocrystalline (NC) materials are a class of materials with complex microstructure characterized by a large grain boundary (GB) interface to volume ratio [35]. NC materials have an average grain size smaller than 100 nm. They can be synthesized using inert gas condensation, mechanical alloying, electrodeposition, crystallization from an amorphous state, or by severe plastic deformation [36].

If the diffusion mean free path of a defect is comparable to the grain size, a defect can readily diffuse to a nearby GB [37]. This suggests that defects can be absorbed and annihilated if grains are small and the total area of intergranular interfaces per unit volume is large. Denuded zones with visibly lower defect density are often observed near GBs in neutron irradiated tungsten [25], helium irradiated iron [38], copper [39], and other materials. Mathematical models [40], treating thermal diffusion of defects and representing GBs by dislocation arrays, explain the variation of defect density as a function of grain diameter. Although here we do not study helium accumulation, we note that GBs can trap a considerable amount of helium [41,42]. GB networks also provide pathways for the rapid diffusion of hydrogen [43].

[*]Contact author: leo_ma55@hotmail.com
[†]Contact author: daniel.mason@ukaea.uk
[‡]Contact author: steven.van.boxel@ukaea.uk
[§]Contact author: sergei.dudarev@ukaea.uk; sergei.dudarev@linacre.ox.ac.uk

NC materials generally exhibit higher strength but lower ductility [44]. GBs resist the propagation of dislocations and raise the yield strength through the Hall-Petch effect. Atomistic simulations of NC copper with the average grain size varying from 3.3 to 6.6 nm show softening in the small grain size limit [45]. Plastic deformation in this case is mediated by small-scale events of GB sliding, known as the inverse Hall-Petch effect occurring if the grains are too small to accommodate multiple dislocations. NC copper with a bimodal grain size distribution, involving both nano- and micrometer grains, exhibits both high strength and high ductility [44].

Radiation resistance of NC and ultrafine grain tungsten was investigated by El-Atwani *et al.* [46] using heavy ion Si, Cu, and W irradiation. They found that the density of defects increases gradually at low doses, followed by a higher defect production rate at intermediate doses and saturation at high doses. The density of defects starts decreasing from the dose of ∼3 dpa. El-Atwani *et al.* [46] proposed that this stems from the coalescence of defects and the absorption of small defect clusters by the GBs. They also found that defect densities were independent of grain size in the grain size range from 60 to 400 nm. The more recent carbon ion irradiation experiments performed at room temperature and at 1050 K, with doses varying from 0.25 to 4 dpa, showed that NC tungsten exhibited lower void swelling than coarse-grained tungsten [47]. Voids shrank in the high dpa limit, where vacancy loops were observed instead. El-Atwani *et al.* [48] also analyzed tungsten containing equiaxial 35 nm and 85 nm NC grains, ultrafine 100–500 nm coexisting grains, and large grains in the 1–3 μm size range. After exposure to Kr ion irradiation at room temperature and 800 °C, the NC samples exhibited a pattern of damage similar to that observed in the ultrafine grain samples.

Using Kr ion irradiation, Rose *et al.* [49] found that in NC Pd and ZrO_2, where the grain size distribution spanned the range from 10 to 300 nm, the density of defects was lower in the small grain size limit. Dey *et al.* [50], in similar ion irradiation experiments on yttria-stabilized zirconia with grain sizes of 25, 38, and 220 nm, found higher defect densities in the large grain size samples. In the small grain samples, no interstitial type defects were observed, suggesting that the defects were fully absorbed by the GBs. The growth of small grains was also observed and attributed to radiation defect-induced GB migration, not detected for large grains.

Atomic scale simulations [51–54] suggest that GBs act as sinks for radiation defects, in particular interstitial-type defects. Using molecular statics (MS), Tschopp *et al.* [52] evaluated the formation energies of self-interstitial and vacancy defects near a GB and found that they were different from the corresponding bulk values. MD simulations of a copper bicrystal showed that GBs absorbed collision cascade-induced stacking fault tetrahedra [55,56]. GBs were also shown to be able to emit interstitial-type defects that then annihilate with vacancies [53].

The above atomic-scale studies show that GBs are not sessile sinks for radiation defects but instead they are dynamic regions interacting with, and absorbing, defects through the reconfiguration of local atomic GB structures. Simulations also show that whereas an interstitial cluster can be absorbed by a GB, resulting in a local translation of the GB plane, self-interstitial defects approaching a GB from both sides produce a compensating effect.

Fluctuations of GB structure due to its interaction with radiation-induced defects give rise to grain coarsening [57–60]. Wang *et al.* [58] found that the average grain diameter varied linearly as a function of radiation dose in the low dose limit. At high doses, the rate of grain growth slows down [59,60]. Using Vineyard's thermal spike concept [61], Kaoumi *et al.* [57] developed a rate theory model predicting that the average grain size $\bar{d}_g$ varies as a function of dose φ as $\bar{d}_g^3(\varphi) - \bar{d}_g^3(0) \propto \varphi$. This result appears consistent with the available observations, but it has not yet been examined using direct atomic scale simulations.

Examples of large-scale atomic-scale simulations involving multiple grains in a sample exposed to radiation are rare. Levo *et al.* [62] performed collision cascade simulations of NC nickel and multicomponent alloys, simulating thousands of cascades in cells containing 446 000 atoms and 10 grains, and observing radiation-induced grain coarsening. Comparing simulations by Levo *et al.* [62] with the work by Granberg *et al.* [63], we deduce that the dose accumulated in simulations by Levo *et al.* [62] was in the 0.2 to 1 dpa range. This illustrates the challenges involved in a simulation of the effect of grain size on the evolution of a material under irradiation in the limit of high radiation exposure.

Performing collision cascade simulations [14,64] still requires extensive use of supercomputer time to accumulate a dose exceeding 1 dpa. As an alternative, we explore the effect of NC grain structure in the limit of high exposure using the creation-relaxation algorithm (CRA) [11]. CRA is a robust algorithm enabling the exploration of microstructural evolution in the limit of high radiation exposure. The algorithm generates defective structures by randomly selecting and replacing atoms in a material, followed by the structural relaxation of resulting atomic configurations, and is conceptually similar to the Frenkel pairs accumulation (FPA) [65] method. The evolution of microstructure simulated using the CRA is driven solely by the spatially fluctuating stress fields of radiation defects. CRA simulations have recently been verified by a direct comparison of the predicted pattern of microstructural evolution [11] with the evolution observed in ion irradiation experiments, exhibiting good agreement between theory and observations [15].

Here, we examine the evolution of microstructure and swelling in NC tungsten simulated using the CRA over a broad range of radiation exposure, extending the analysis given in our preliminary publication [66], in which we outlined some basic elements of the approach but did not investigate the observed phenomena at any depth. The new analysis of simulation data presented below alters the interpretation of results in comparison with the evaluation given in Ref. [66] and explains why the samples with smaller grains exhibit lower swelling at high exposure and why a NC material reaches the asymptotic dynamic steady state at a higher dose than a single crystalline material. We find that the higher resistance to swelling in the low grain size limit results from the combined effect of the initial excess volume associated with disordered grain boundary regions and the high integral volume of the grain boundary defect-denuded zones. Furthermore, because of the spatial constraints that a polycrystalline

TABLE I. Initial parameters of grains in the simulated NC tungsten samples.

Index	Cell size (a^3)	No. of grains	$\langle V \rangle$ (nm^3)	St. dev. of V (nm^3)	Tr. junc. per vol^{-1} (nm^{-2})	GB area per vol^{-1} (nm^{-1})	Grain diameter d_c (nm)
1	$80 \times 80 \times 80$	242	65.713	27.715	1.075	1.444	5.0
2	$80 \times 80 \times 80$	71	223.979	86.800	0.478	0.965	7.5
3	$80 \times 80 \times 80$	30	530.083	193.513	0.268	0.720	10.0
4	$80 \times 80 \times 80$	15	1060.165	401.534	0.169	0.571	12.7
5	$120 \times 120 \times 120$	30	1789.028	600.558	0.119	0.483	15.1
6	$120 \times 120 \times 120$	12	4472.572	1773.687	0.066	0.358	20.4

topology imposes on the evolution of microstructure, where the grain boundaries impede the formation of an extended percolating dislocation network, the dislocation structures emerging under irradiation are restricted to isolated dislocation loop configurations.

II. THEORY

A. Simulation cells

Simulation cells with equiaxial grains were created using the Voronoi tessellation method implemented in the ATOMSK code [67]. Six sets of simulation cells were produced, with varying numbers of three-dimensional grains and cell sizes. Each set included five independent samples for statistical data analysis. Details of the initial setup are given in Table I. Cell dimensions are given in the units of the equilibrium lattice constant $a = 3.143$ Å of the Marinica EAM4 potential [68]. We have also created perfect crystal cells with the same dimensions and five independent perfect crystalline samples were investigated as reference structures. All the results shown below are averages over five samples representative of a particular realization of microstructure. The error bars represent standard deviations evaluated using the same five samples.

First, we select the size of the simulation cell and the number of grains. The position and crystallographic orientation of grains are assigned randomly. Voronoi polyhedra are generated and filled with atoms assuming a perfect bcc crystal structure. Periodic boundary conditions are applied to the entire cell. A sequential search of atoms with neighbors situated closer than 2 Å is performed and such atoms are deleted to eliminate configurations potentially involving undesired defects in the initial state of the system. As a result, each simulation cell contains a different number of atoms, but the dimensions of all the cells are comparable with the dimensions of cells with perfect crystal structure.

The initial properties of the cells are assessed using the Voronoi polyhedra method. Assuming that a Voronoi polyhedron represents a grain, we evaluate the average and standard deviation of the grain volume and the GB area per unit volume. These parameters are computed using the VORO++ code [69]. The characteristic diameter of a grain d_c is evaluated from the average volume of the grain, in the spherical grain approximation.

In Fig. 1, we plotted histograms of volumes of grains approximated by Voronoi polyhedra. Five different colors represent grains identified in the samples. The brown dotted lines show the probability distribution for the volume of polyhedra V created by the Voronoi tessellation in three dimensions [70], approximated by the equation

$$p(y) = \frac{3125}{24} y^4 \exp(-5y), \tag{1}$$

where $y = V/\langle V \rangle$ and $\langle \ldots \rangle$ denotes taking a statistical average. Taking into account the grain volume distributions in all five samples, the histograms are reasonably well approximated by Eq. (1). This defines the initial conditions for the subsequent simulations of random polycrystals.

Atomic configurations were relaxed using two many-body tungsten potentials, the Marinica EAM4 potential [68] and the Mason-NguyenManh-Becquart (MNB) potential [71]. First, conjugate gradient relaxation was performed using fixed volume cells, applying the convergence criterion for the maximum force on an atom of 0.01 eV/Å. Then, we thermalized the samples by integrating Langevin equations of motion of atoms over 1 ns, where the temperature of the Langevin thermostat was set to 300 K. Subsequently, the cells were allowed to change their volumes and shape through interaction with a barostat to a stress-free condition, with further thermalization applied over a further 1 ns. Over this second time interval, the temperature of the Langevin thermostat was reduced linearly from 300 K to 0 K. Finally, following Ref. [72], the cell shape and volume were relaxed using the conjugate gradient method with the maximum force convergence criterion of 1×10^{-8} eV/Å. All the MD and MS calculations described in this study were carried out using LAMMPS [73,74].

Since the amount of data generated using the above procedure is very large, in what follows we shall focus on analyzing simulations performed using the MNB potential. Results derived from the Marinica EAM4 potential are qualitatively similar but exhibit higher defect densities, in agreement with the published studies [11].

Some of the data noted in this paper were presented in Ref. [66]. We have since expanded the data set and carried out a detailed examination of the entire amount of data in the study below.

B. Creation-relaxation algorithm

The creation-relaxation algorithm (CRA) [11] enables a computationally efficient generation of atomic-scale microstructures resembling those observed in the high dose limit [15]. It is a robust parameter-free algorithm, where the

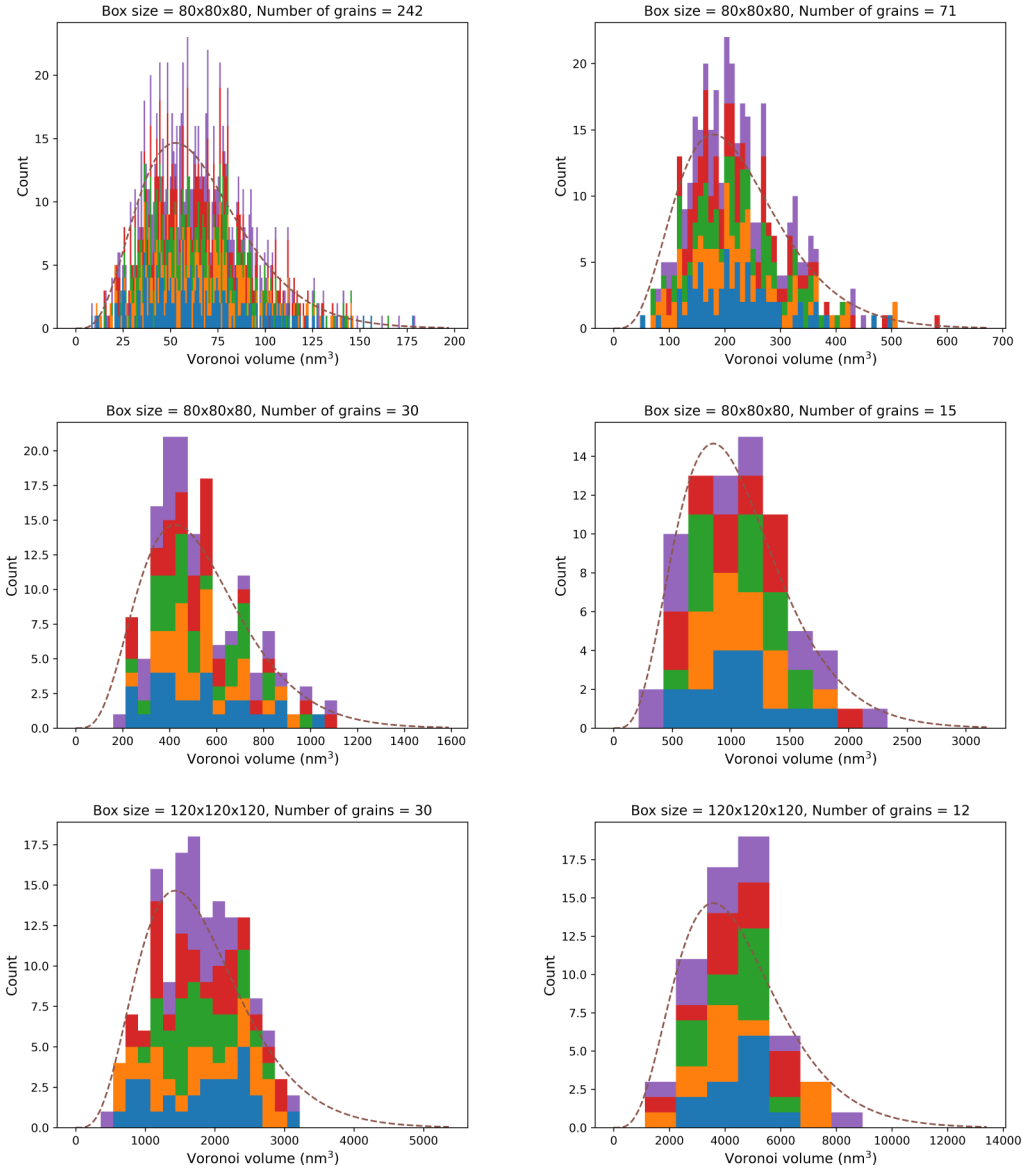

FIG. 1. Histograms of grain sizes in the simulation samples of various cell sizes and number of grains. In each histogram, the number of bins is the same as the number of grains and in each case the data are derived from five representative samples.

algorithm itself enables introducing a mechanistic definition for the displacement per atom (DPA) parameter.

Starting with an initial atomic configuration, which in this study is a polycrystal, a small number of atoms n are removed from their original positions and then reinserted in the structure randomly within the simulation cell. The resulting configuration is then relaxed using the conjugate gradient method to a zero-stress state, completing a cycle of the CRA algorithm. In each cycle, the dose is incremented by n/N cDPA, where N is the total number of atoms in the simulation cell. The mechanistic canonical definition of the displacement per atom parameter cDPA [11] is independent of the structure of the material and applies to crystalline as well as noncrystalline configurations considered below. It is physically similar to the conventional definition of NRT-DPA [75] proportional to the "damage" energy delivered to the material by an energetic particle. While the initial version of the CRA algorithm [11] involved generating a single Frenkel pair per algorithmic step ($n = 1$), several subsequent studies [12,13,76] showed that, in a large simulation cell, it is computationally more efficient to displace several atoms per cycle at a rate approximately equal to 0.001 cDPA per cycle. Below, we accumulate 0.001 cDPA per algorithmic cycle and repeat the simulations until the desired dose of several dpa is reached.

The conditions of validity of the CRA algorithm have been extensively explored elsewhere [11,77]. It is sufficient to say that predictions generated using the algorithm are in good qualitative agreement with experimental observations [15] if the rate of thermal relaxation of microstructure is low in comparison with the rate of generation of radiation defects. In many cases the relaxation rates span hours [78] or even months [79], making the CRA algorithm suitable for simulating the evolution of materials under irradiation at ambient and even elevated temperature conditions [77].

C. Atomic-level characterization of grain boundaries

Other than using the initial Voronoi polyhedra, there is no unique way to assign an atom to a particular grain. Atoms at grain boundaries (GBs) generally cannot be identified as being a part of any particular crystal structure. It is not even possible to specify the width of a GB without ambiguity. Derlet *et al.* [72] inspected the pair distribution function of atoms near a GB in NC nickel and separated atoms into three categories: an atom in a positionally disordered environment, an atom associated with a lattice site of a neighboring fcc grain, and a bulk atom. They also concluded that the nature of a GB in an NC material is similar to that of a GB in a polycrystal. Due to the ambiguity of the definition of the width of a GB, identifying the location of a GB also involves an element of uncertainty. This then translates into the uncertainty of the definition of the volume of a grain, the GB area, and triple junctions in atomic-scale simulations.

OVITO [80] provides a means for performing grain segmentation, where grains are identified in three steps. First, the local atomic structure and orientation are determined through polyhedral template matching (PTM) [81]. Then, a nondirected graph representation is created, where each atom is treated as a graph node and each bond as a graph edge. Finally, grains are formed through a hierarchical clustering of the graphs. The procedure involves an element of empiricism and can identify grains, but provides no means for evaluating the GB area.

For this study, we extended the OVITO algorithm by identifying the local environments of atoms in the crystal and cluster regions with similar orientations and then associating atoms with similar environments into grains. The main difference with the original OVITO algorithms is that an orientation of the environment is now determined by best-fitting the local atomic structure to the third nearest neighbors and that atoms are classified according to a strict majority rule, i.e., an atom is assigned to grain g if more than half of its neighbors are. The algorithm is slower than the PTM but more robust if lattice defects are present. The classification procedure leaves a small number of atoms in highly disordered regions with no grain index. Starting from grain indices and atomic positions, GBs are then defined as triangulated surfaces between the grains. With this definition, the GB area is simply the sum of areas of the triangles making up the GB surface, the grain volume is computed as a surface integral using the divergence theorem, and the distance from an arbitrary point to a GB is the distance to the nearest triangle.

D. Vacancy and void detection

In an NC simulation where the GBs themselves are mobile, the detection of defects using the conventional Wigner-Seitz defect analysis involving fixed reference lattice sites is challenging. In Ref. [82], a new void detection method was developed that is transferable to heavily irradiated NC materials. As a brief summary, a scalar phase field, $\phi(\mathbf{r})$, is evaluated at each point $\mathbf{r} \in \mathcal{R}^3$ in the simulation cell, defined as the distance of $\mathbf{r}$ to the nearest atom, scaled such that $\phi = 0$ on an atom and $\phi = 1$ on the surface of a (locally oriented and strained) Wigner-Seitz cell. Regions $\phi > 1$ are deemed void space. As we can also find the distance $d(\mathbf{r})$ from a point to the nearest GB surface, we can therefore find the regions where both $\phi > 1$ and $d > d_c$. Thus we can find the volume of void space more than a distance d_c from a GB and then the density of void space as a function of distance from a GB.

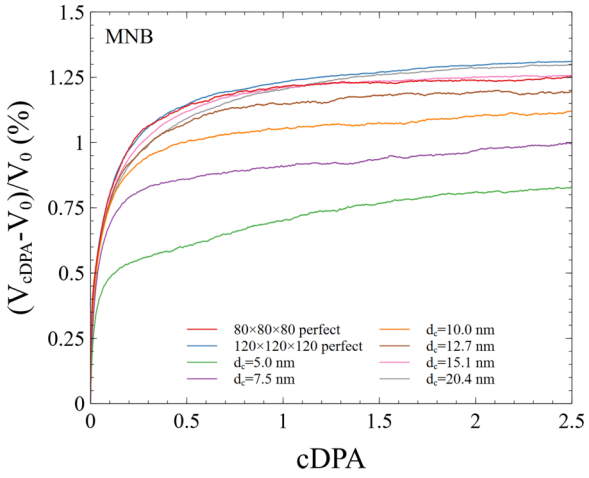

FIG. 2. Volume of the simulation cells as a function of dose, expressed in the cDPA units. The initial characteristic diameter of grains d_c is related to the average grain volume in the spherical grain approximation. This figure illustrates the details of the transient approach to dynamic equilibrium as a function of grain size. Some data in this figure have been reproduced from [66].

III. RESULTS AND ANALYSIS

A. Radiation induced swelling

Figure 2 illustrates one of the central results of this study showing the relative change in the volume of the simulation cell as a function of dose for the various initial grain sizes. The simulations were performed under stress-free conditions, achieved through the relaxation of cell boundaries. Figure 2 shows that swelling is substantially lower in polycrystalline materials with initially smaller grains. While the predicted volume change depends on the interatomic potential used in simulations, the qualitative variation of swelling as a functional of dose and microstructure is generic.

As the dose increases, the cell volume saturates at ∼1 cDPA for the single crystal and large grain size systems. This is consistent with earlier analyses of high dose effects in tungsten, iron, and zirconium [11–13,76,77]. The saturation of swelling in a single crystal stems from the accumulation of a high, spatially homogeneous, concentration of vacancies and the coalescence of self-interstitial defects into an extended dislocation network.

According to Fig. 2, a material with a more complex microstructure appears more resistant to irradiation-induced swelling compared to a single crystalline material. Neutron irradiation experiments on ferritic steels [22,31] suggest that, in microstructurally complex materials, there is an incubation dose interval where swelling is suppressed, as opposed to simple alloys where swelling starts almost immediately at a low dose [13,77]. Small grain size materials exhibit a trend similar to that found in observations.

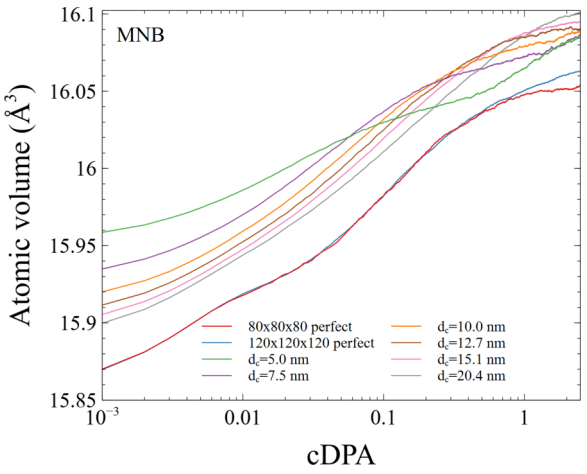

FIG. 3. Average volume per atom in NC microstructures computed for materials with varying grain size, shown as a function of dose, given in cDPA units. The grains with the average diameter below ∼7.5 nm exhibit a significantly slower rate of evolution with dose, bearing in mind the logarithmic scale of variation of the horizontal axis. Some data in this figure have been reproduced from [66].

A distinct aspect of a NC material is that there are two contributions to swelling—one stemming from the GBs themselves and the other from the defects produced by irradiation. Both contributions vary as a function of dose. Figure 3 shows the evolution of the average volume per atom in a NC sample as a function of dose. Initially, the volume per atom is anticorrelated with the grain size, owing to the higher volume density of GB in the smaller grain size limit. Materials swell monotonically as a function of dose because lattice defects typically have larger effective volumes than atoms in a single crystal. In a single crystalline material, swelling stems from the accumulation of lattice defects alone, but in a NC material, the volume increase is mitigated by the interaction between GBs and defects, leading to the smallest grain samples exhibiting the lowest relative volume increase.

Simulations extending to a large, but still finite, dose illustrated in Fig. 3 shows that the average volume per atom in a NC material reaches a higher value than in a single crystal. This stems from the fact that GBs themselves are defects, with the associated extra volume explicitly visible at zero exposure in Fig. 3. The simultaneous presence of GBs and radiation defects gives rise to a higher total volume per atom value in a NC material than in an irradiated single crystal. In applications, what matters is the difference between the volume per atom

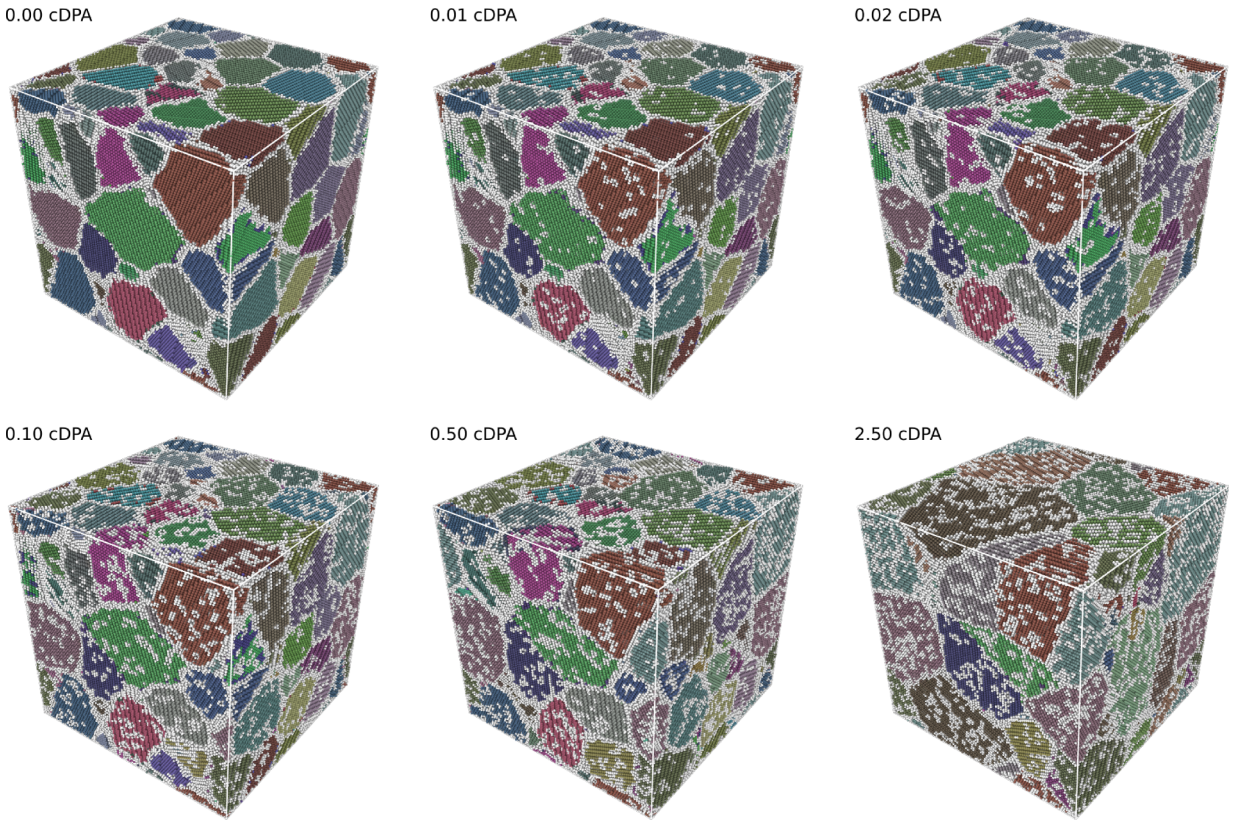

FIG. 4. Nanocrystalline atomic structures exposed to various doses, defined by the respective cDPA values, and visualized using OVITO [80]. Initially, the simulation cell contains approximately $80 \times 80 \times 80$ bcc unit cells and 71 grains with the average grain diameter $d_c = 7.5$ nm. Simulations were performed using the MNB interatomic potential. Atoms are colored according to the structure of their crystallographic neighborhood, with atoms in non-bcc environments shown in white. Note that the polycrystalline sample used in this study is different from that used in Ref. [66].

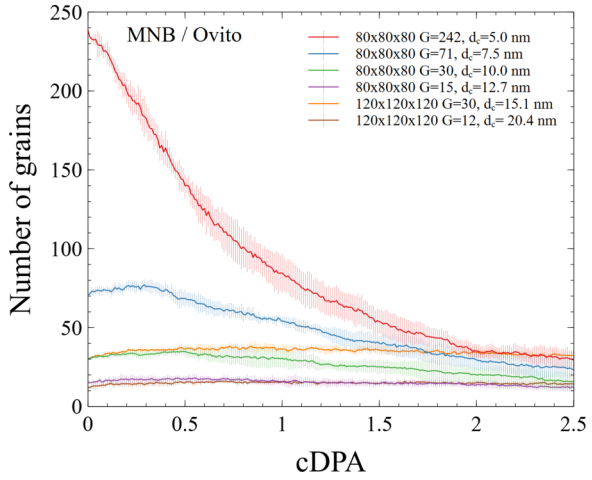

FIG. 5. Number of grains in an irradiated NC sample evaluated using OVITO and plotted as a function of cDPA.

value in an initial structure and in the same structure exposed to irradiation. This difference is systematically lower in an irradiated NC material in comparison with a single crystal.

B. Evolution of grain structure

The morphology of grain structure in a NC sample changes due to the interaction between GBs and radiation defects.

Figure 4 illustrates the evolution of grain structure in NC tungsten with the initial grain diameter of $d_c = 7.5$ nm. The color of an atom refers to its local crystallographic environment determined by the PTM method. As defects accumulate, grains change shape, split, or merge.

Figure 5 shows the number of grains as a function of dose, where the grains were identified using the OVITO algorithm. For comparison, in Fig. 6 we plotted the number of grains evaluated using the algorithm described in Sec. II C and detailed in Ref. [66]. The results shown in the two figures agree very well.

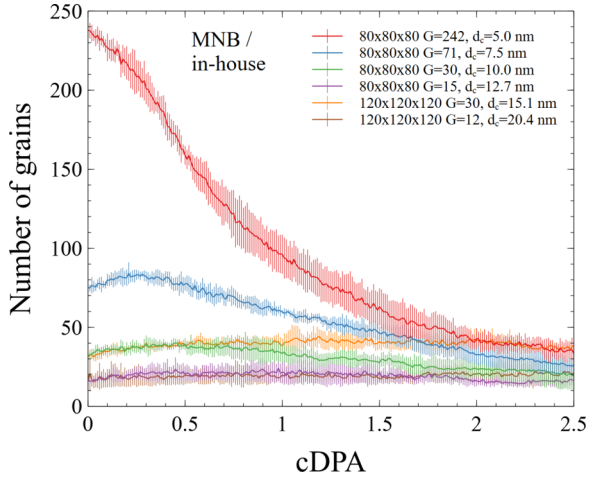

FIG. 6. Number of grains in an irradiated NC sample evaluated using a method described in Sec. II C and plotted as a function of cDPA. Some data in this figure have been reproduced from [66].

In the nanostructures involving the initial average grain size of $d_c = 5.0$ nm, the number of grains decreases steadily with dose. For grains with $d_c = 7.5$ nm, there is a slight increase in the grain count at approximately 0.3 cDPA, followed by grain coarsening at higher doses. Similarly, for $d_c = 10.0$ nm, the grain count is maximum at around 1.2 cDPA. In the samples with the largest grains, the number of grains fluctuates but remains nearly constant.

The grain coarsening observed above agrees with results by Levo *et al.* [62], who simulated collision cascade exposure of nickel and nickel-based multicomponent alloys with a grain size of 10 nm. Other studies [51–56] illustrated how GBs interact with defects and move through local atomic rearrangements.

Zhang *et al.* [83] observed the evolution of NC zirconia with grain sizes in the range from 5 to 10 nm following exposure to 2 MeV Au ions to doses up to 35 DPA at temperatures of 160 K and 400 K. Observations showed that the average grain size increases approximately to 30 nm at 35 DPA. Zhang *et al.* [83] noted that the radiation-induced grain growth did not involve thermal activation, as slower grain growth was observed at 400 K compared to 160 K. Broadly similar observations were reported by Dey *et al.* [50], who observed the growth of small grains (25 nm and 38 nm) and attributed the effect to radiation defect-induced GB migration. The above observations agree with our simulations showing that NC materials are susceptible to grain coarsening under irradiation.

In our grain segmentation analysis, we assumed the minimum size of a grain to be equal to 100 atoms. In experiments, there is a visibility limit, implying that grains below a certain size may remain undetected. By examining experimental data [58,60,84], we infer that the visibility limit approximately equals 5 nm. Disregarding the small grain sizes accounting for the volume fraction of less than 1%, and focusing only on the grains larger than 5 nm, we find that the predicted grain size distribution exhibits grain coarsening similar to that observed in experiments.

Analysis of ion irradiation experiments [85] suggests that the average grain diameter, treated as a function of dose, follows a power law

$$\bar{d_g}^n(\varphi) - \bar{d_g}^n(0) \propto \varphi, \tag{2}$$

where φ is the dose and $1.9 < n < 4.3$. Kaoumi *et al.* [57] developed a thermal spike model suggesting that $n = 3$, in broad agreement with observations. Neutron irradiated NC copper [84] also shows a sublinear increase of d_g as a function of dose. A subtle aspect of the interpretation of observations, revealed by the simulations, is that grain visibility affects the counting and identification of grains.

In Fig. 7, the average diameter of grains is plotted as a function of dose, with grains in the range $d_g < 5.0$ nm, representing a small volume fraction of the total, not included in the analysis. The figure exhibits a steady increase of the average grain size; however, there is no evidence that this increase follows a power law. The difference between simulations and experimental observations [57] likely stems from the fact that the CRA simulations do not account for the effect of thermal diffusion of defects, treated in the thermal spike model.

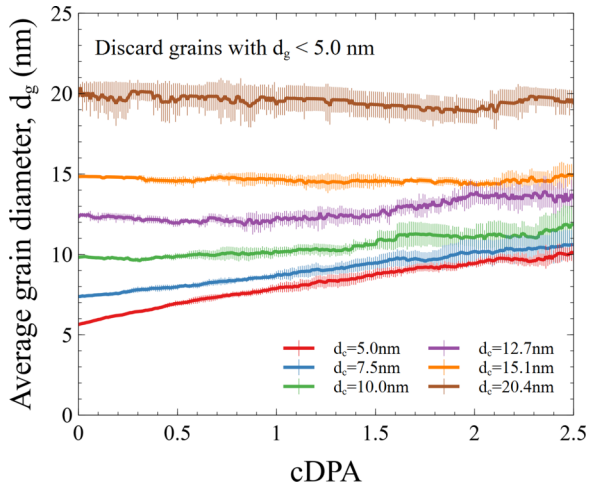

FIG. 7. Average grain diameter plotted as a function of cDPA with grain diameters smaller than 5.0 nm excluded from the analysis.

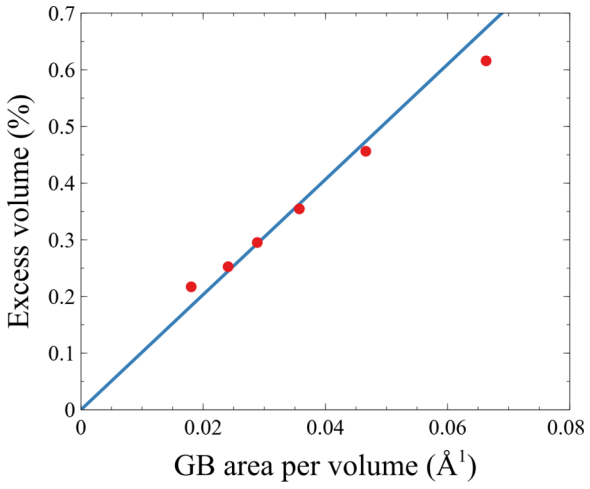

FIG. 9. Excess volume versus GB area per unit volume. The data are taken from Figs. 3 and 8 at zero cDPA. A linear fit is shown as a guide for an eye.

The variation of the total GB area as a function of dose is shown in Fig. 8, illustrating that the GB area decreases monotonically as a function of dose. A comparison of the GB area at zero dose to the volume per atom at the same zero dose in Fig. 3 enables estimating the excess volume associated with GBs. This excess volume is plotted in Fig. 9 as a function of GB area. The fact that the plot is nearly linear shows that the excess volume per unit GB area is a constant and the slope of the curve provides a measure of structural imperfection of local atomic GB structure. This also shows that, as the total GB area decreases at high doses, the proportion of the excess volume associated with GBs in Fig. 3 is decreasing.

C. Dislocation density

Dislocation loops and extended dislocation networks form in CRA simulations by the agglomeration of self-interstitial atom defects. In the absence of thermally activated diffusion, this agglomeration is driven by lattice strains produced by the defects and is energetically highly favorable since the incorporation of a self-interstitial defect into a dislocation loop releases energy comparable with the formation energy of a self-interstitial atom defect [86]. The evolution of the dislocation component of microstructure in a single crystal is illustrated in Fig. 10. The most notable aspect of evolution is the formation of a system-spanning dislocation network, the emergence of which represents a percolating transition in an ensemble of growing and coalescing dislocation loops [87].

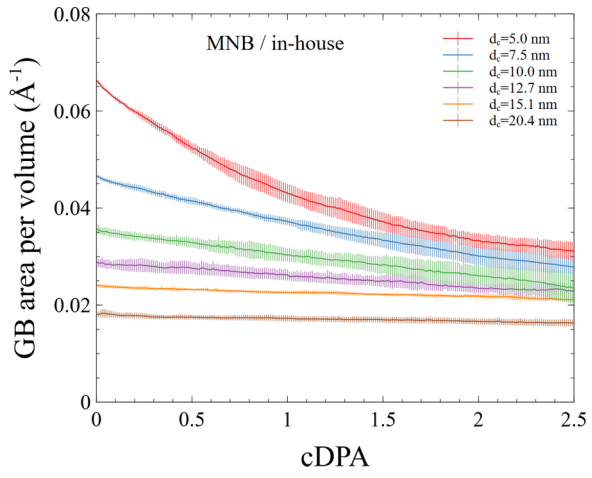

FIG. 8. Grain boundary area per unit volume plotted as a function of cDPA. Some data in this figure have been reproduced from [66].

A low-angle GB can be treated as a regular array of dislocations [88,89], and the dislocation extraction algorithm (DXA) [90] duly detects dislocations in GBs. In Sec. II C we defined a GB as a triangulated surface and also defined the shortest distance from atom to GB, $d(\mathbf{r})$. To make a meaningful dislocation analysis of irradiated NC structures and exclude the dislocations associated with GBs themselves, we have eliminated all the atoms within 1 Å of a GB before performing a DXA analysis.

Figure 11 illustrates the evolution of a NC system under irradiation. The initial trend in the accumulation of dislocations is similar to that observed in a single crystal. Dislocation loops form and grow over the dose interval extending to 0.2 cDPA, Following that, the density of dislocations starts decreasing, in agreement with observations [77].

A distinct feature of dislocation microstructure evolution in a NC material is the impeded formation of an extended dislocation network at high doses. Indeed, in a NC material, a dislocation line is not able to simply traverse across a grain boundary. Instead, dislocation lines terminate at GBs. As a result, the dominant dislocation feature observed in NC samples is the dislocation loops situated in the interior of the grains.

To quantify the evolution of dislocation microstructure in a NC material, we computed the dislocation line density as a function of dose. The results are plotted in Fig. 12. The dislocation line density in a NC material is lower than in an irradiated single crystal. Furthermore, the formation of an extended system-spanning dislocation network is suppressed, resulting in the dislocation line density rapidly reaching saturation and not exhibiting the characteristic peak often found in simulations of single crystals [11,65,77].

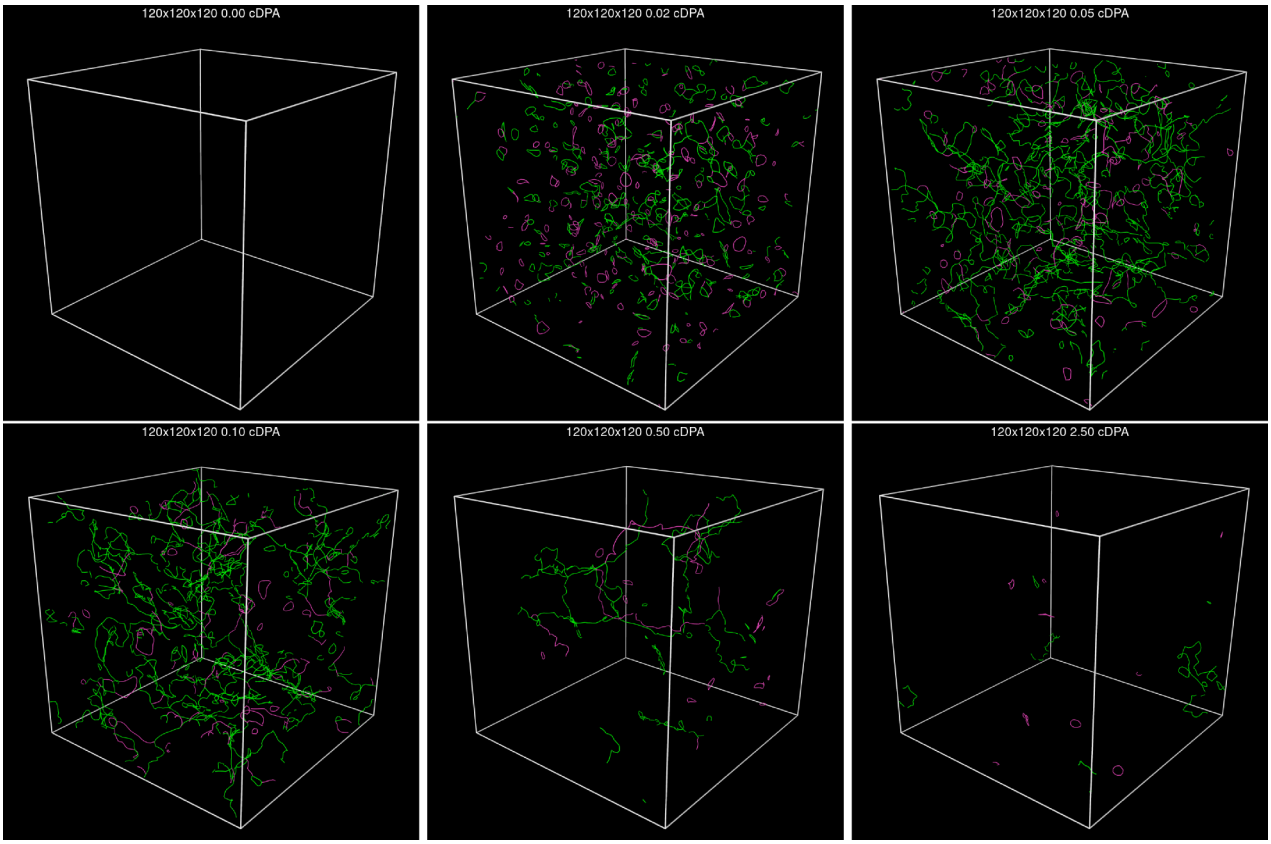

FIG. 10. Dislocations detected by DXA in a single crystal sample containing 120 × 120 × 120 bcc unit cells and simulated using the MNB potential. Green lines represent dislocation with the $\frac{1}{2}\langle 111\rangle$-type Burgers vector; magenta lines are the dislocations with the $\langle 001\rangle$-type Burgers vector. An extended system-spanning percolating dislocation network forms at $\varphi \sim 0.3$ cDPA.

It is appropriate to pose a question about how the statistically averaged dislocation line density varies as a function of distance to a GB, given the extensive observation of defect-denuded zones adjacent to GBs [38]. Figure 13 shows an example of the distribution of dislocation line density evaluated by eliminating the atoms separated from GBs by a distance smaller than d. The total dislocation line length is denoted by L_d and the corresponding volume is denoted by V_d. The high values corresponding to the interval of d between 0 and 1 Å stem from the identification of GBs with arrays of dislocations. To avoid ambiguities, we use the cutoff distance d of 1 Å to define the dislocation density in the bulk of the grains.

The density of dislocations in the various regions of the grains was determined by selecting the appropriate values of L_d and V_d. Dislocation density in a region separated by distance d from a GB, where $d = 2.5$ Å, is shown in Fig. 14. Data points with d below 1 Å were excluded from the analysis. In the samples with smaller grain sizes, the formation of dislocation line objects is suppressed. However, as the grain size increases, dislocations start forming in the interior of the grains, while their occurrence in the vicinity of GBs is still suppressed. Figure 14 shows a zone near GBs that is depleted of dislocations, with the width of the zone varying from 10 to 20 Å.

The occurrence of dislocation denuded zones and fluctuating dislocation content in NC grains was observed in a variety of experimental studies. El-Atwani *et al.* [47] performed 3 MeV Cu^+ ion irradiation experiments on tungsten samples, in which the microstructure contained 100 nm and 100–500 nm grains, as well as larger grains exceeding 1 μm in size. The NC samples typically exhibited a lower density of dislocation loops at room temperature. In a separate investigation of irradiated Fe films, El-Atwani *et al.* [38] found that the dislocation loop density increased as a function of grain size in the grains below 100 nm in diameter. Denuded zones were observed near GBs and the width of the denuded zones varied in the 5 to 8 nm range in the grains where such denuded zones were detected.

In this study, the occurrence of dislocation denuded zones in the vicinity of GBs was observed systematically in all cases and the width of the denuded zone was relatively small. At finite temperatures, the thermally activated mobility and thermal fluctuations of grain boundaries should likely increase the width of denuded zones. The formation of denuded zones at low temperatures is driven by stress and involves local rearrangements of atomic configurations of grain boundaries associated with the absorption and emission of defects.

D. Density of vacancies and voids

Vacancies and voids (v + v) represent a fundamental class of defect objects produced by irradiation. The nucleation and growth of voids is a prominent manifestation of radiation swelling [91]. The evolution of v + v defects in NC

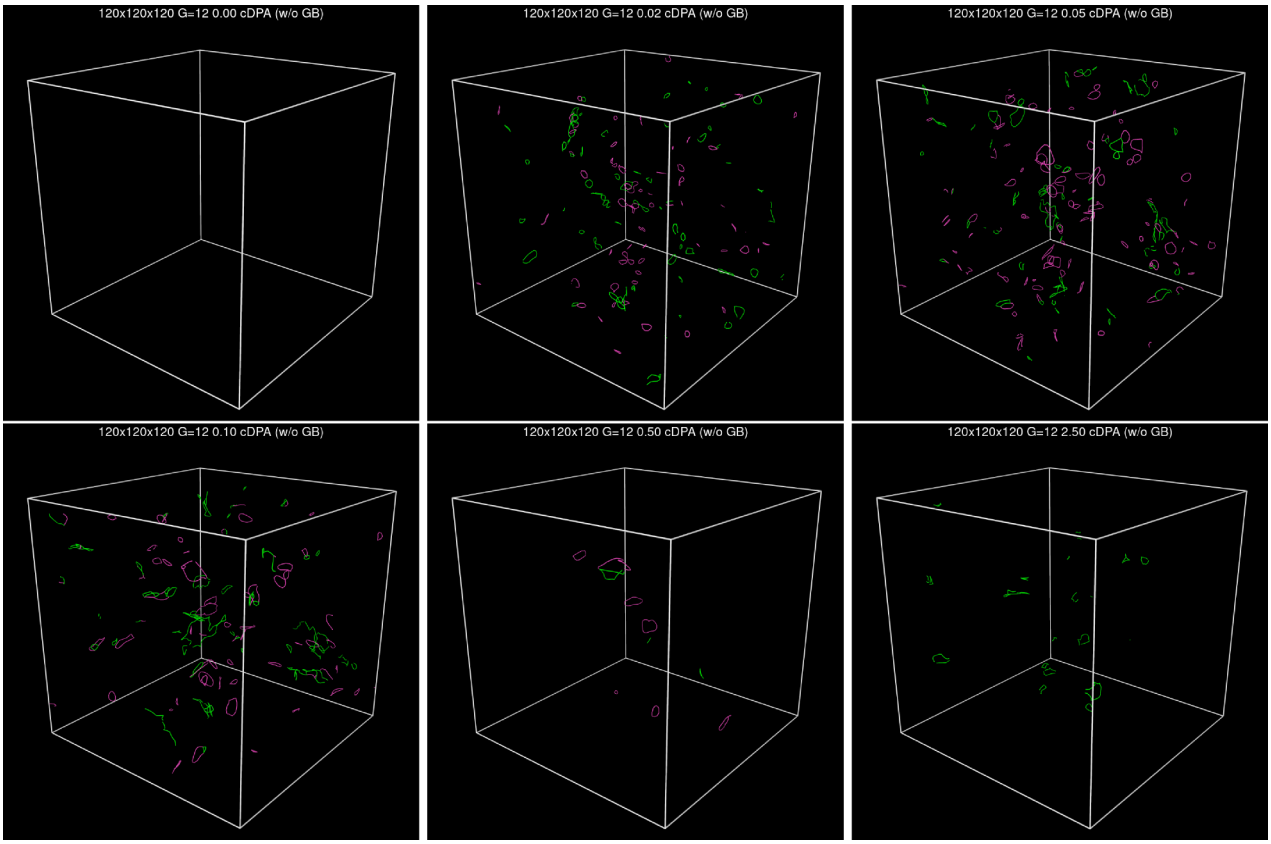

FIG. 11. Dislocation detected by DXA in a NC sample with $d_c = 20.4$ nm containing the equivalent of $120 \times 120 \times 120$ bcc unit cells simulated using the MNB potential. Atoms separated from GB by a distance smaller than 1 Å were removed before applying the DXA. The topology of the grain microstructure prevents the formation of a dislocation network, impeding the dislocation percolating transition [87] even in the high dose limit.

materials differs from that observed in single crystals, reducing swelling.

In a perfect crystal, the Wigner-Seitz analysis provides a straightforward means for identifying self-interstitial and vacancy defects. The analysis involves comparing the defective structure to a reference single crystal structure and identifying the defects by counting the number of atoms within a Voronoi cell centered on an atom in the reference lattice. In a NC material, however, matching a reference structure to a grain containing defects is difficult because of the spatial variation of crystal orientation, even within the same grain. The accumulation of defects and grain coarsening gives rise to further

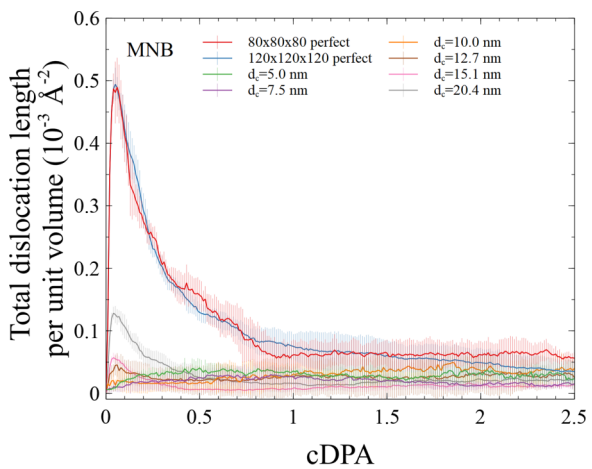

FIG. 12. Total dislocation length per unit volume as a function of cDPA. Atoms separated from GBs by less than 1 Å are removed from the analysis before the application of the DXA.

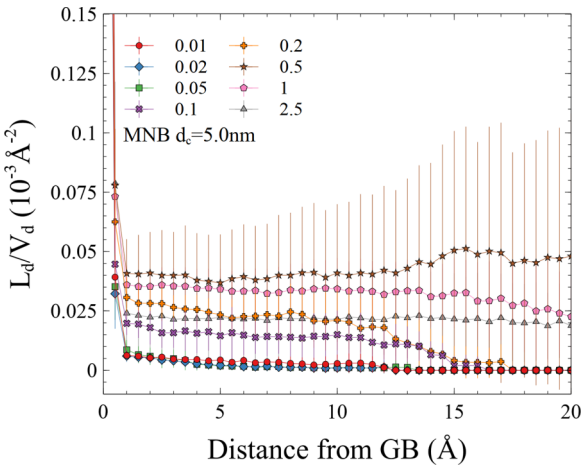

FIG. 13. Total dislocation line length L_d in volume V_d, where atoms with distance from GB smaller than d are eliminated from the analysis. Simulations were performed using the MNB potential.

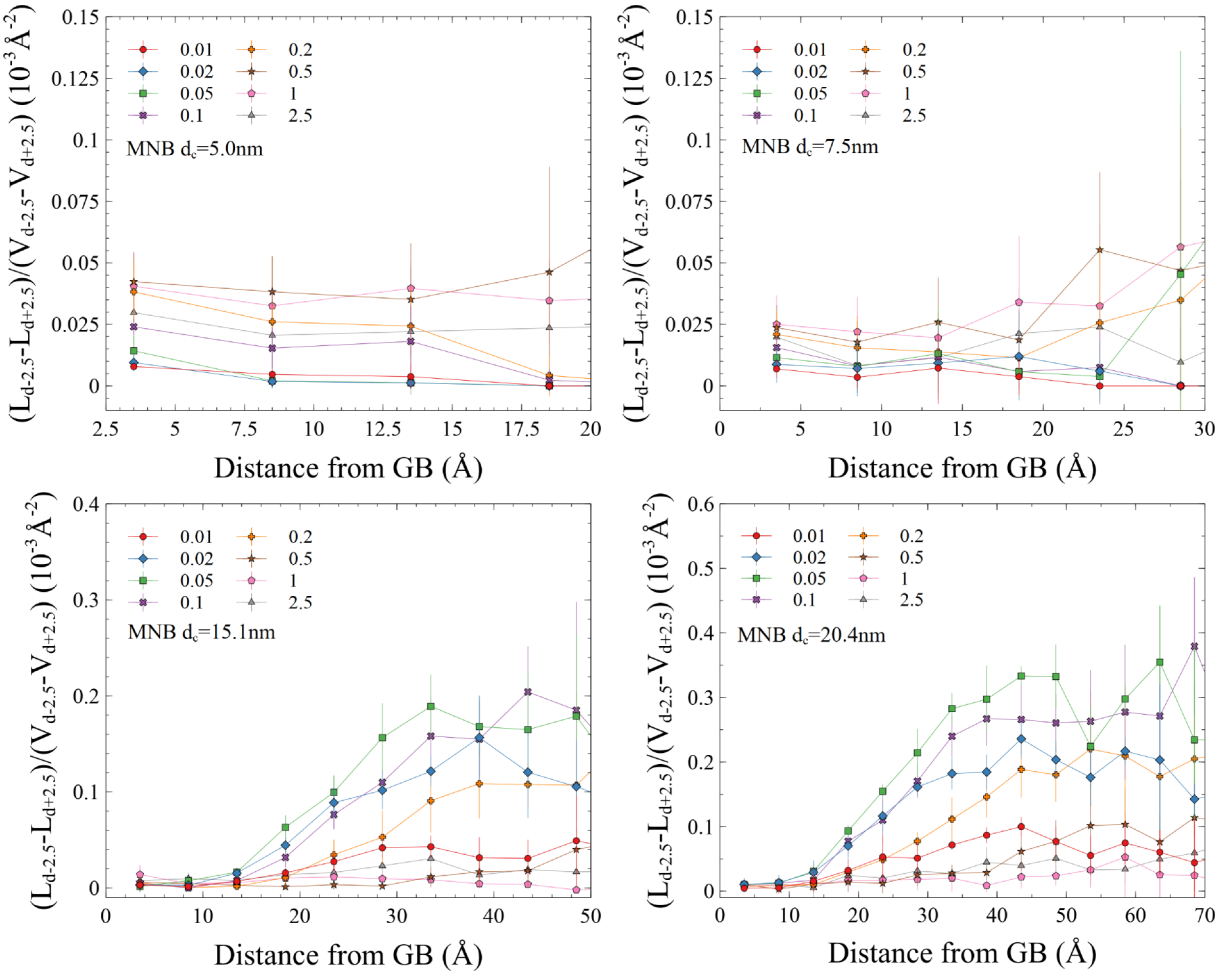

FIG. 14. Dislocation density plotted as a function of distance from the nearest GB, with the dose in cDPA units indicated in the legend against the corresponding curve. Smaller grains exhibit low dislocation density even at high radiation exposure, whereas larger grains develop regions containing a high density of dislocations in the interior of the grains. Simulations were performed using the MNB potential.

changes in crystal orientation. As a consequence, the use of the Wigner-Seitz analysis does not appear applicable in the context of this study.

An alternative algorithm developed by Mason *et al.* [82] was applied to the identification of vacancies and voids. The algorithm enables determining the size and spatial distribution of vacancies and vacancy clusters and computing v + v concentrations at various distances from a GB.

Figure 15 shows the variation of the total v + v volume in a simulation cell as a function of cDPA. The v + v volumes computed for single crystal configurations vary similarly to what was found earlier by Derlet and Dudarev [11]. Samples with smaller grains tend to show lower v + v volumes, in agreement with observations showing reduced swelling found in NC materials. We note that the variation of cell volume illustrated in Fig. 2 also includes the excess volume associated with the GBs themselves, making the interpretation of the volumetric strain data more complex than in single crystalline samples.

Figure 16 provides a visual representation of the morphology of vacancies and voids in the interior of the grains and at GBs. Voids in the grain interior have a more spherical shape, whereas those in close proximity of GBs exhibit somewhat greater shape irregularity. The latter can be attributed to the increased structural disorder in the crystal structure near GBs.

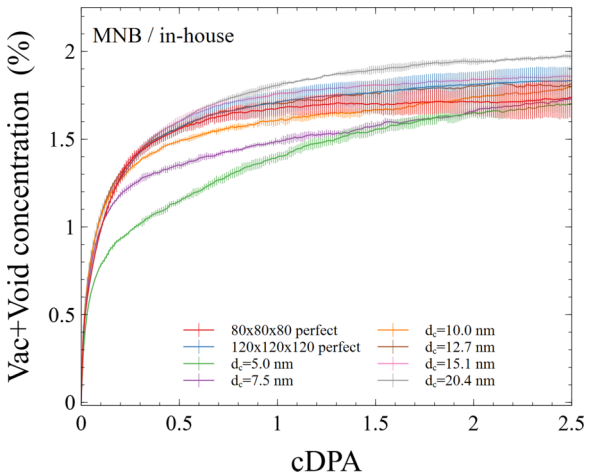

FIG. 15. Total content of vacancies and voids per unit volume as a function of cDPA. Some data in this figure have been reproduced from [66].

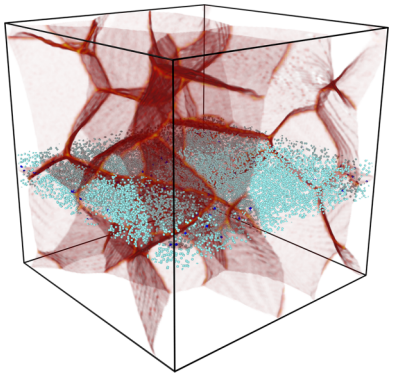

FIG. 16. Microstructure of vacancies and voids in a NC sample with the initial grain diameter of $d_c = 20.4$ nm and the simulation cell size equivalent to 120 × 120 × 120 unit cells at 2.5 cDPA. Vacancies and voids are only shown in a slice of the simulation cell. Voids situated in the interior of the grains are shown in light blue and those situated in the immediate vicinity of GBs are shown in deep blue. Simulations were performed using the MNB potential.

Furthermore, vacancies and voids are distributed throughout the interior of the grains, particularly at higher doses. In the simulations performed using the Marinica EAM4 potential, voids are predominantly found near GBs.

Spatial distributions of vacancies and voids exhibit consistent trends as functions of distance from a GB and radiation exposure. Figure 17 shows v + v concentrations plotted as functions of distance from a GB. The profiles are derived by calculating the v + v content in a region defined by its distance to the nearest GB. A v + v denuded zone is observed in the vicinity of every GB, extending to ∼10 Å, with a notable change of slope in the concentration of v + v at around 10 Å. Since in a CRA simulation vacancy diffusion does not occur, the presence of a vacancy and void denuded zone is associated with the lattice deformation-mediated interaction rather than diffusion [92]. The width of the denuded zone appears to be independent of grain size. In the limit of small grain size corresponding to the greater dominance of GBs, the volume-average concentration of vacancies and voids is lower, in agreement with the data shown in Fig. 15.

Klimenkov *et al.* [93] and Dürrschnabel *et al.* [25] examined the distributions of voids in tungsten exposed to neutron irradiation to 1.6 DPA at 900 °C and to 1 DPA at 800 °C. These observations identified void denuded zones near GBs, extending to approximately 15–25 nm, followed by a region where void concentration was higher. Notably, these observations referred to the range of high temperatures where vacancies are highly mobile, making a direct comparison with low temperature CRA simulations not possible; however, the qualitative trends found in experiments are similar to those found in simulations.

E. Potential energy

One of the advantages offered by molecular dynamics simulations is that they enable computing the potential energy of every atom. Figure 18 shows the spatial distribution of the potential energy of atoms for the structures shown in Fig. 4, with the atoms now color-coded according to their potential energy. The images show that GBs and defects correspond to higher potential energy of atoms. As the radiation damage accumulates, the overall potential energy of the material increases, in agreement with experimental observations [94].

The potential energy of atoms at GBs and in the grain interior is shown in Fig. 19, where it is evaluated using a distance bin size of 0.5 Å. To ensure physical consistency, the range of abscissas in the plot is capped at approximately one-third of d_c for the corresponding system. The distance-average potential energy is maximum at the GB and gradually reaches saturation beyond the distance of 10 Å. A higher dose corresponds to a higher value of the potential energy at saturation. A feature consistently observed in all the simulations is a potential energy minimum at a relatively small distance from a GB at high doses. The factors contributing to this phenomenon are attributed to two effects. First, the local lattice structure is distorted at the GB, resulting in a maximum of the potential energy at 0 Å, which gradually vanishes at

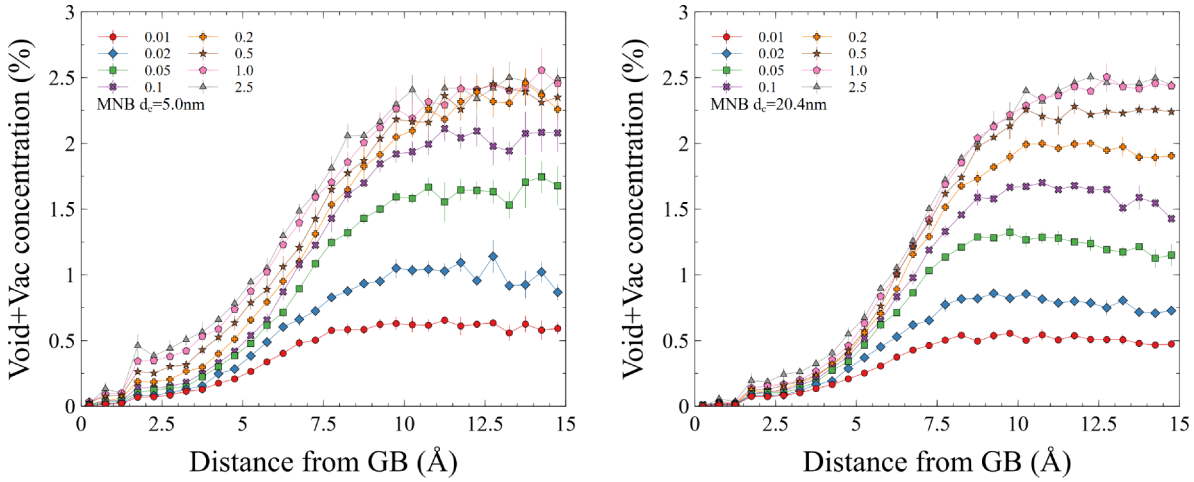

FIG. 17. Concentration of vacancies and voids as a function of distance from GBs, with the dose in cDPA units indicated in the legend against the corresponding curves. Note the similarity between the curves referring to the smallest and largest grain sizes. Simulations were performed using the MNB potential.

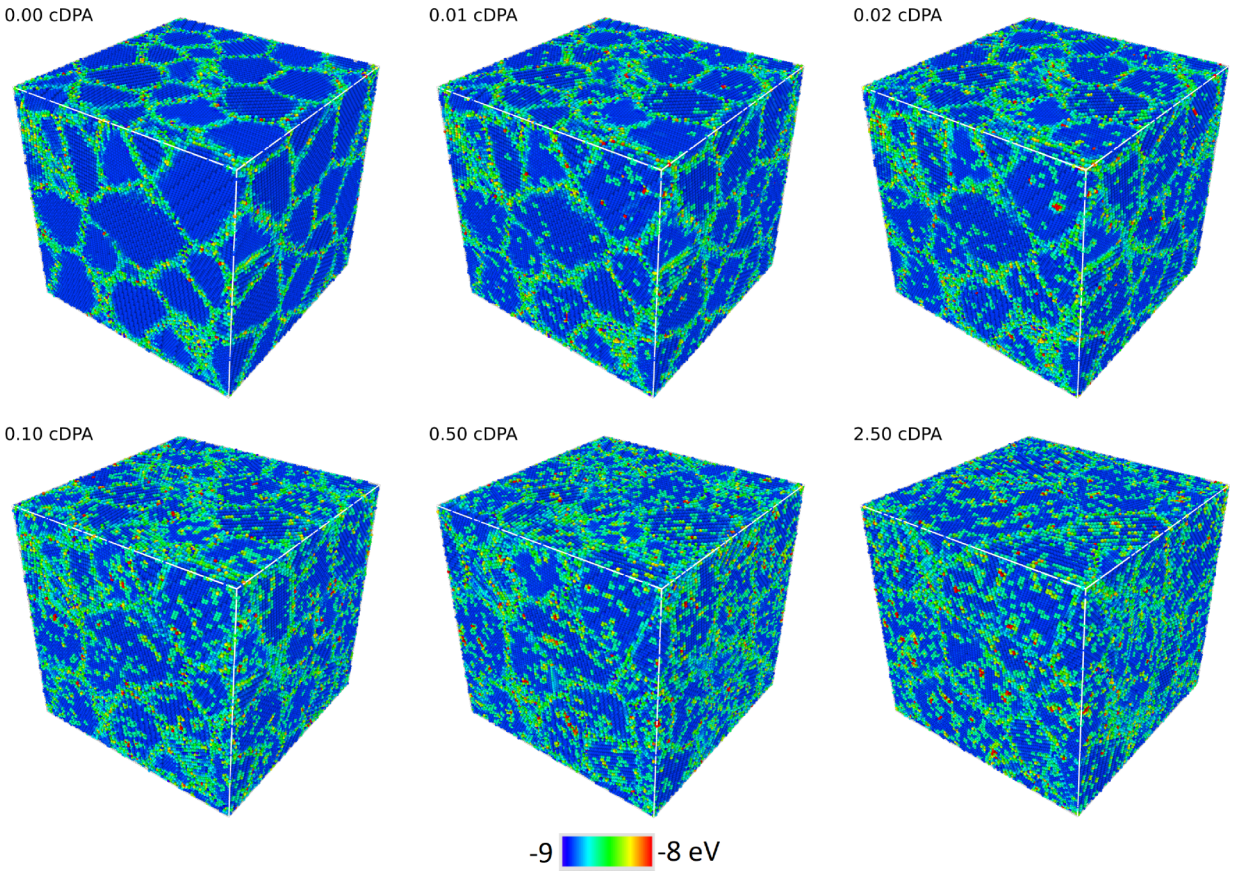

FIG. 18. Atomic configuration similar to those shown in Fig. 4, with the color now referring to the potential energy of atoms in eV units.

the distance of approximately 10 Å; this persists even in the high dose limit. Second, GBs suppress the occurrence of dislocations and vacancies in the denuded zone spanning the distance from 10 to 20 Å. A combination of the two effects results in the formation of a region near a GB where atoms have lower potential energy.

Figure 20 shows how the average potential energy of atoms in the simulation cell varies as a function of dose. In a single crystal, the potential energy increases as defects accumulate, saturating at approximately 0.5 cDPA [11]. By fitting an exponential function to the curve describing a single crystal, we identify the characteristic dose scale of approximately 0.22 cDPA. In an NC system, the potential energy saturates at a higher value compared to a single crystal. This illustrates a substantial energy difference between a NC and a single crystal associated with the presence of GBs where atoms have

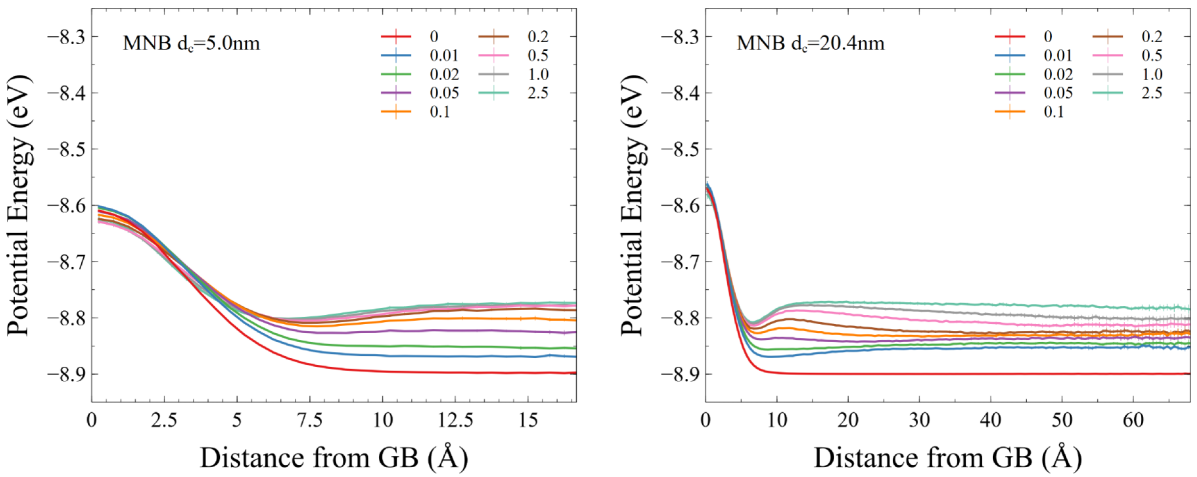

FIG. 19. Average potential energy of atoms plotted as a function of distance from a GB, computed for the samples with the smallest and the largest initial grain size. The dose in cDPA units corresponding to each curve is indicated in the legend. Simulations were performed using the MNB potential.

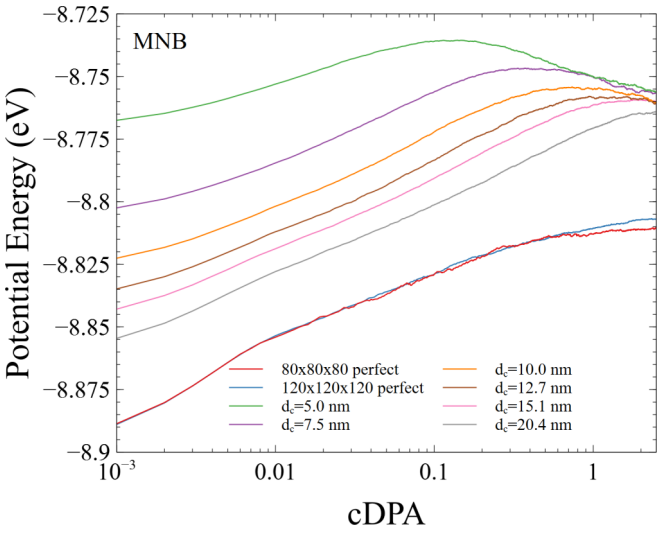

FIG. 20. Volume average potential energy of atoms plotted as a function of dose given in cDPA units.

higher energy because of their noncrystalline local environment.

As the dose increases, the potential energy increases due to the accumulation of defects. In NC samples with small grain sizes of 5.0, 7.5, and 10.0 nm, we observe a distinct pattern with an initial peak followed by a subsequent decrease. The peak occurs earlier in smaller grain size systems. A simple thermodynamic model can be formulated to explain how the potential energy changes with dose. The potential energy can be written as

$$E = E_0 + E_D(\varphi)(1 - \kappa_{GB}A_{GB}) + A_{GB}\gamma_{GB}, \tag{3}$$

where E_0 is the potential energy of atoms in a single crystal lattice, E_D is the additional energy due to the accumulation of defects, $\kappa_{GB}A_{GB}$ is the volume fraction of GB areas with the width comparable with that of the denuded zone, A_{GB} is the total GB area, and γ_{GB} is the GB energy per unit area. Since the energy E_D associated with the accumulation of defects rapidly increases on the dose scale of ~0.2 cDPA, the potential energy initially increases and then gradually diminishes as a result of grain coarsening, associated with the reduction of the GB area.

F. von Mises stress

The von Mises stress (VMS) is often used in engineering for identifying the locations prone to plastic yielding or fracture. The VMS is evaluated using the principle of the maximum distortion energy and is a conveniently positive-semi-definite measure of the overall stress state in a component. The VMS σ_v can be computed from the two principal invariants of the Cauchy stress tensor σ_{ij} [95] to the elements of which it is related *via*

$$\begin{aligned}\sigma_v^2 &= \tfrac{3}{2}\left[(\sigma_{ij}\sigma_{ji}) - \tfrac{1}{3}(\sigma_{ii})^2\right] \\ &= \tfrac{1}{2}\left[(\sigma_{11}-\sigma_{22})^2 + (\sigma_{22}-\sigma_{33})^2 + (\sigma_{33}-\sigma_{11})^2\right. \\ &\quad \left. +6\left(\sigma_{23}^2 + \sigma_{31}^2 + \sigma_{12}^2\right)\right],\end{aligned} \tag{4}$$

where the repeated indices imply summation. We define the *atomic* VMS using the above equation, in which σ_{ij} is the atomic virial stress. This enables examining the spatial distribution of the VMS at atomic resolution.

Figure 21 shows the same GB structure as in Fig. 4, where the color now refers to the atomic VMS stress. Significant stress concentrations are visible at GBs, similarly to how the potential energy of atoms is the highest at the GBs; see Fig. 19. As the radiation defects accumulate, an increasing number of atoms acquire higher VMS values. The GB regions exhibit higher atomic VMS values compared to the defects in the grain interior.

Figure 22 illustrates the nature of stress relaxation in the vicinity of a GB. The VMS at the GB decreases as a function of dose, suggesting that, as defects accumulate and interact with the GB, the level of atomic stress at the GBs relaxes. VMS is minimum from approximately 6 to 10 Å away from a GB. This is likely associated with the formation of defect denuded zones devoid of dislocations and defects.

G. Defect-grain boundaries interaction

The origin of defect-denuded zones and grain coarsening induced by irradiation is attributed to the interaction of irradiation-induced defects with GBs. The defects and GBs have relatively high potential energy, stimulating the relaxation of local atomic environments into lower energy configurations. Local distortions of the lattice and the associated stress concentrations drive the rearrangement of atomic configurations [11–13,76]. Defects formed in a close proximity to a GB are more readily incorporated into the GB structure. This finding agrees with other atomic-scale simulations [51–54] showing that GBs are not static sinks for defects but highly stressed dynamic regions where defect reconfigurations and morphological changes readily occur.

Figure 23 illustrates the evolution of the VMS in an NC sample over a small dose increment spanning the dose from 2.515 cDPA to 2.520 cDPA. Each image in the series corresponds to the dose increment of 0.001 cDPA. Initially, a well-defined defect is visible at the bottom of the figure. In the subsequent frames, the region of higher stress associated with the defect undergoes structural relaxation. The gradual further accumulation of defects elsewhere in the structure causes this local atomic configuration of the defect to become unstable, resulting in the eventual relaxation and reconfiguration into a lower-stress state.

Notably, this simulation does not represent an event of diffusion-mediated motion and absorption of a defect cluster by a GB. Instead, a local atomic configuration undergoes a rearrangement, resulting in a lower overall stress state of the system. This series of images indicates that an interface between a structurally disordered region with high energy per atom (a defect) and a perfect crystalline region acts as a catalyst for defect recombination. GBs, instead of serving as static sinks for defects, are dynamic entities able to absorb, transform, and relax the irradiation-generated defects, hence impeding the indefinite accumulation of radiation effects even in the absence of diffusion.

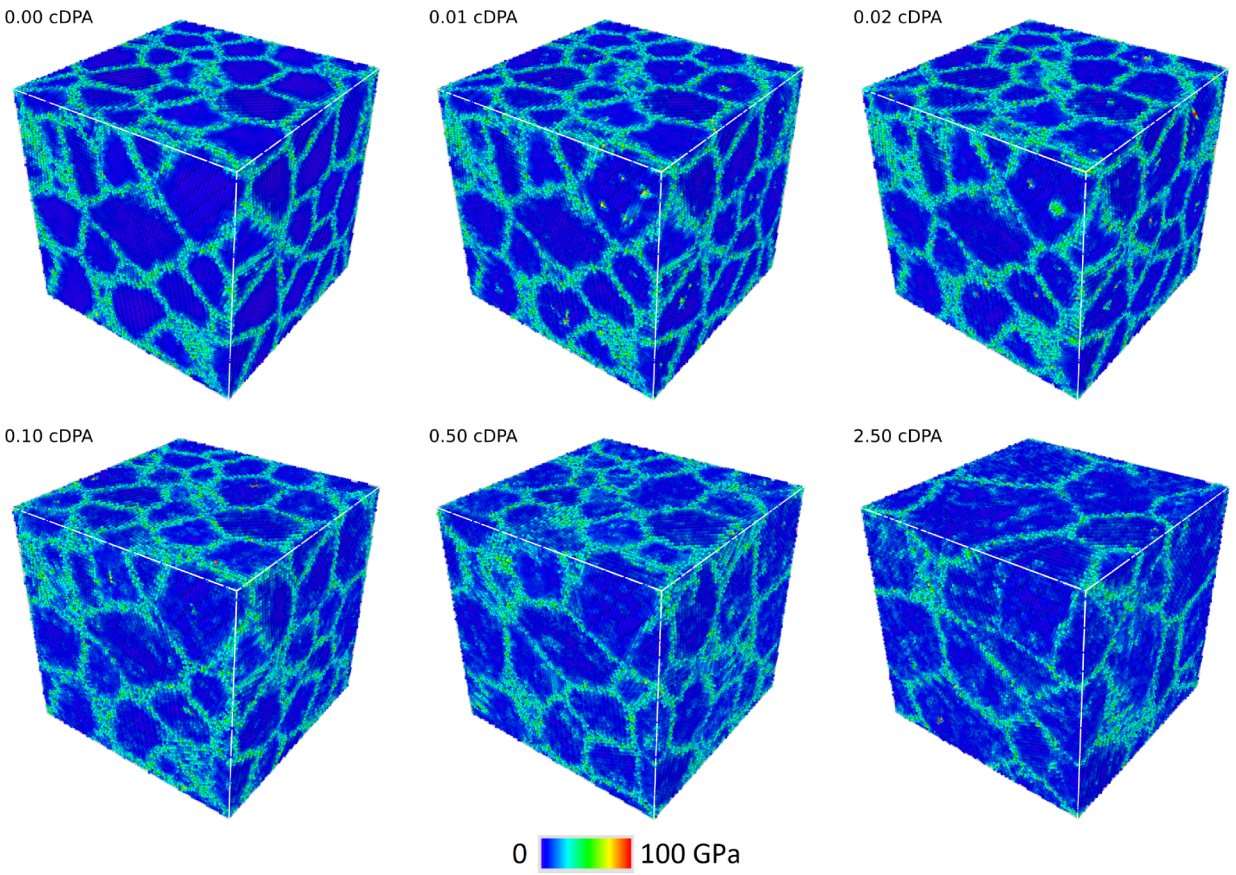

FIG. 21. Atomic configuration similar to those shown in Fig. 4, with the color now referring to the atomically resolved von Mises stress given in the units of GPa.

IV. CONCLUSIONS

Using atomic-scale simulations, we find that, in the athermal limit, a NC tungsten exhibits higher resistance to irradiation-induced swelling compared to a single crystalline material. The formation of an extended system-spanning dislocation network is suppressed by the interaction of dislocations with grain boundaries, resulting in a significantly lower density of dislocations in an irradiated nanocrystalline material. The evolution of a nanocrystalline material as a function of exposure occurs slower than in a single crystalline material. The deceleration stems from the evolution of the grain boundary structures slowly coarsening under radiation exposure. The initial excess

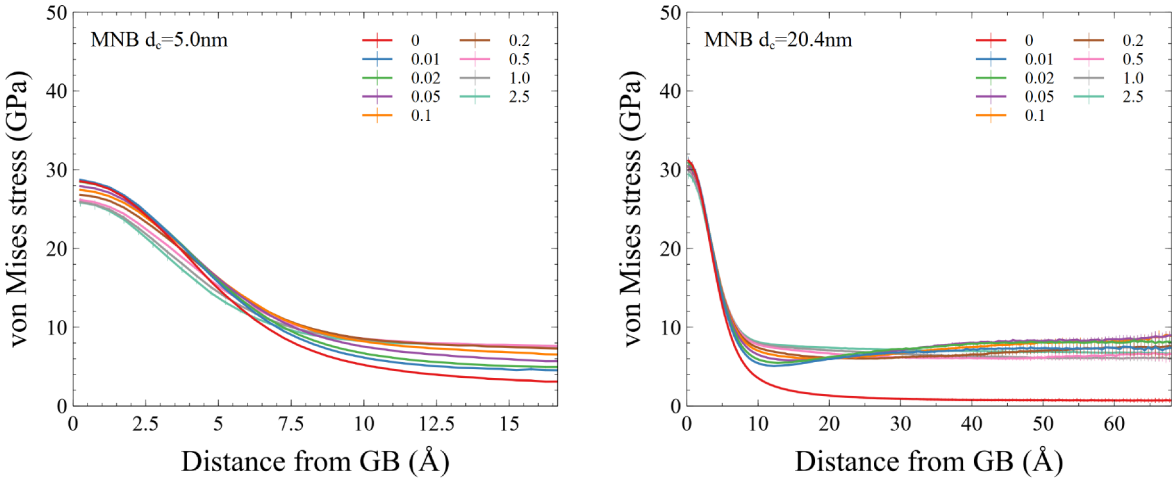

FIG. 22. von Mises stress plotted as a function of distance from a GB, computed for the samples with the smallest and the largest initial grain size. The dose in cDPA units corresponding to each curve is indicated in the legend. Simulations were performed using the MNB potential.

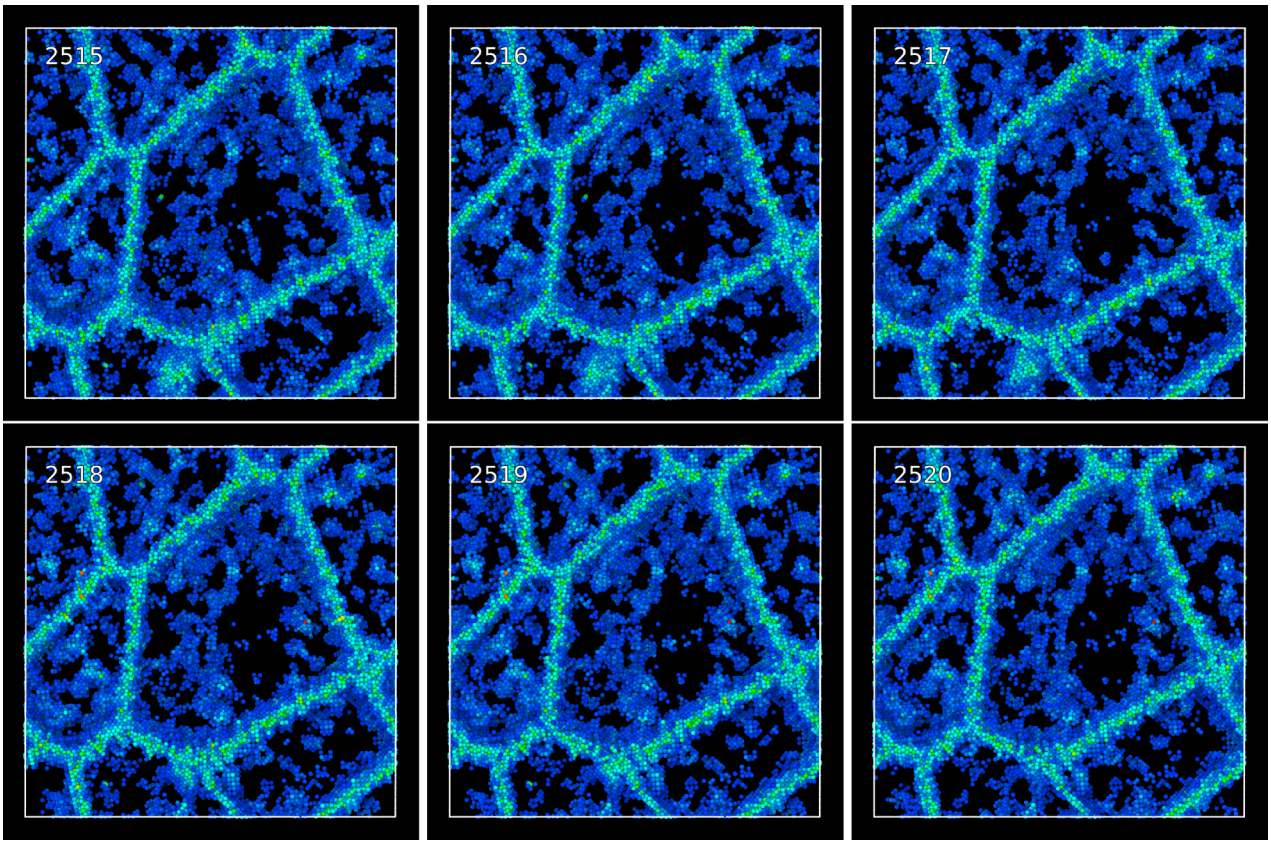

FIG. 23. Spatial distribution of the VMS in a sample with the initial average grain diameter of $d_c = 10$ nm. The images show atomic VMS in a rectangular slab with a thickness of 15 Å to highlight the distribution of defects at a greater level of resolution in comparison with Ref. [66]. Atoms with a VMS lower than 10 GPa are not shown. The images correspond to the CRA steps from 2515 to 2520, which are equivalent to the variation of dose from 2.515 to 2.520 cDPA. A defect cluster at the bottom of the images interacts with a GB and gets incorporated into it. The color scheme is the same as in Fig. 21.

volume associated with grain boundaries and the lattice-deformation-mediated interaction between grain boundaries and defects also reduces the magnitude of volumetric strain that radiation exposure produces in a nanocrystalline material.

Further information on the data and models underlying this paper are available [96].

ACKNOWLEDGMENTS

This work has been carried out within the framework of the EUROfusion Consortium, funded by the European Union via the Euratom Research and Training Programme (Grant Agreement No. 101052200—EUROfusion) and from the UK EPSRC Energy Programme (Grant No. EP/W006839/1), and was partially supported by the Broader Approach Phase II agreement under the PA of IFERC2-T2PA02. We gratefully acknowledge the provision of computing resources by the IRIS (STFC) Consortium. We also acknowledge EUROFusion for the provision of access to Marconi and Marconi100 supercomputer facility at CINECA, Bologna, Italy.

Views and opinions expressed are however those of the authors only and do not necessarily reflect those of the European Union or the European Commission. Neither the European Union nor the European Commission can be held responsible for them.

[1] G. Federici, L. Boccaccini, F. Cismondi, M. Gasparotto, Y. Poitevin, and I. Ricapito, An overview of the EU breeding blanket design strategy as an integral part of the DEMO design effort, Fusion Eng. Des. **141**, 30 (2019).

[2] J. H. You, E. Visca, C. Bachmann, T. Barrett, F. Crescenzi, M. Fursdon, H. Greuner, D. Guilhem, P. Languille, M. Li, S. McIntosh, A. V. Müller, J. Reiser, M. Richou, and M. Rieth, European DEMO divertor target: Operational requirements and material-design interface, Nucl. Mater. Energy **9**, 171 (2016).

[3] G. Federici, C. Skinner, J. Brooks, J. Coad, C. Grisolia, A. Haasz, A. Hassanein, V. Philipps, C. Pitcher, J. Roth, W. Wampler, and D. Whyte, Plasma - material interactions in current tokamaks and their implications for next step fusion reactors, Nucl. Fusion **41**, 1967 (2001).

[4] M. R. Gilbert and J.-C. Sublet, Neutron-induced transmutation effects in W and W-alloys in a fusion environment, Nucl. Fusion **51**, 043005 (2011).

[5] S. Sato and K. Maki, Analytical representation for neutron streaming through slits in fusion reactor blanket by Monte Carlo calculation, Fusion Eng. Des. **65**, 501 (2003).

[6] L. Reali, M. R. Gilbert, M. Boleininger, and S. L. Dudarev, Intense γ-photon and high-energy electron production by neutron irradiation: effects of nuclear excitations on transport of defects, PRX Energy **2**, 023008 (2023).

[7] A. E. Sand, S. L. Dudarev, and K. Nordlund, High-energy collision cascades in tungsten: Dislocation loops structure and clustering scaling laws, Europhys. Lett. **103**, 46003 (2013).

[8] X. Yi, A. E. Sand, D. R. Mason, M. A. Kirk, S. G. Roberts, K. Nordlund, and S. L. Dudarev, Direct observation of size scaling and elastic interaction between nano-scale defects in collision cascades, Europhys. Lett. **110**, 36001 (2015).

[9] A. E. Sand, D. R. Mason, A. D. Backer, X. Yi, S. L. Dudarev, and K. Nordlund, Cascade fragmentation: deviation from power law in primary radiation damage, Mater. Res. Lett. **5**, 357 (2017).

[10] K. Nordlund, S. J. Zinkle, A. E. Sand, F. Granberg, R. S. Averback, R. Stoller, T. Suzudo, L. Malerba, F. Banhart, W. J. Weber, F. Willaime, S. L. Dudarev, and D. Simeone, Improving atomic displacement and replacement calculations with physically realistic damage models, Nat. Commun. **9**, 1084 (2018).

[11] P. M. Derlet and S. L. Dudarev, Microscopic structure of a heavily irradiated material, Phys. Rev. Mater. **4**, 023605 (2020).

[12] D. R. Mason, S. Das, P. M. Derlet, S. L. Dudarev, A. J. London, H. Yu, N. W. Phillips, D. Yang, K. Mizohata, R. Xu, and F. Hofmann, Observation of transient and asymptotic driven structural states of tungsten exposed to radiation, Phys. Rev. Lett. **125**, 225503 (2020).

[13] A. R. Warwick, M. Boleininger, and S. L. Dudarev, Microstructural complexity and dimensional changes in heavily irradiated zirconium, Phys. Rev. Mater. **5**, 113604 (2021).

[14] M. Boleininger, D. R. Mason, A. E. Sand, and S. L. Dudarev, Microstructure of a heavily irradiated metal exposed to a spectrum of atomic recoils, Sci. Rep. **13**, 1684 (2023).

[15] S. Wang, W. Guo, T. Schwarz-Selinger, Y. Yuan, L. Ge, L. Cheng, X. Zhang, X. Cao, E. Fu, and G.-H. Lu, Dynamic equilibrium of displacement damage defects in heavy-ion irradiated tungsten, Acta Mater. **244**, 118578 (2023).

[16] F. Hofmann, D. R. Mason, J. K. Eliason, A. A. Maznev, K. A. Nelson, and S. L. Dudarev, Non-contact measurement of thermal diffusivity in ion-implanted nuclear materials, Sci. Rep. **5**, 16042 (2015).

[17] S. Cui, R. P. Doerner, M. J. Simmonds, C. Xu, Y. Wang, E. Dechaumphai, E. Fu, G. R. Tynan, and R. Chen, Thermal conductivity degradation and recovery in ion beam damaged tungsten at different temperature, J. Nucl. Mater. **511**, 141 (2018), special section on 18th International Conference on Fusion Reactor Materials.

[18] A. Reza, H. Yu, K. Mizohata, and F. Hofmann, Thermal diffusivity degradation and point defect density in self-ion implanted tungsten, Acta Mater. **193**, 270 (2020).

[19] A. Hasegawa, M. Fukuda, S. Nogami, and K. Yabuuchi, Neutron irradiation effects on tungsten materials, Fusion Eng. Des. **89**, 1568 (2014), *Proceedings of the 11th International Symposium on Fusion Nuclear Technology-11 (ISFNT-11) Barcelona*, Spain, 2013.

[20] M. Durrand-Charre, *Microstructure of Steels and Cast Irons* (Springer-Verlag, Berlin, 2003).

[21] J. Matolich, H. Nahm, and J. Moteff, Swelling in neutron irradiated tungsten and tungsten-25 percent rhenium, Scr. Metall. **8**, 837 (1974).

[22] F. A. Garner, M. B. Toloczko, and B. H. Sencer, Comparison of swelling and irradiation creep behavior of fcc-austenitic and bcc-ferritic/martensitic alloys at high neutron exposure, J. Nucl. Mater. **276**, 123 (2000).

[23] R. A. Holt, Mechanisms of irradiation growth of alpha-zirconium alloys, J. Nucl. Mater. **159**, 310 (1988).

[24] S. J. Zinkle and J. T. Busby, Structural materials for fission & fusion energy, Mater. Today **12**, 12 (2009).

[25] M. Dürrschnabel, M. Klimenkov, U. Jäntsch, M. Rieth, H. C. Schneider, and D. Terentyev, New insights into microstructure of neutron-irradiated tungsten, Sci. Rep. **11**, 7572 (2021).

[26] M. Boleininger, S. L. Dudarev, D. R. Mason, and E. Martínez, Volume of a dislocation network, Phys. Rev. Mater. **6**, 063601 (2022).

[27] M. L. Jenkins and M. A. Kirk, *Characterization of Radiation Damage by Transmission Electron Microscopy* (Institute of Physics, Bristol, 2001).

[28] Z. Zhou, M. L. Jenkins, S. L. Dudarev, A. P. Sutton, and M. A. Kirk, Simulations of weak-beam diffraction contrast images of dislocation loops by the many-beam Howie–Basinski equations, Philos. Mag. **86**, 4851 (2006).

[29] C. N. Taylor, M. Shimada, B. J. Merrill, M. W. Drigert, D. W. Akers, and Y. Hatano, Development of positron annihilation spectroscopy for characterizing neutron irradiated tungsten, Phys. Scr. **2014**, 014055 (2014).

[30] Z. Hu, P. Desgardin, C. Genevois, J. Joseph, B. Décamps, R. Schäublin, and M.-F. Barthe, Effect of purity on the vacancy defects induced in self–irradiated tungsten: A combination of PAS and TEM, J. Nucl. Mater. **556**, 153175 (2021).

[31] J.-L. Boutard, A. Alamo, R. Lindau, and M. Rieth, Fissile core and tritium-breeding blanket: structural materials and their requirements, C. R. Phys. **9**, 287 (2007).

[32] C. Cabet, F. Dalle, E. Gaganidze, J. Henry, and H. Tanigawa, Ferritic-martensitic steels for fission and fusion applications, J. Nucl. Mater. **523**, 510 (2019).

[33] S. Chang, K.-K. Tseng, T.-Y. Yang, D.-S. Chao, J.-W. Yeh, and J.-H. Liang, Irradiation-induced swelling and hardening in hfnbtatizr refractory high-entropy alloy, Mater. Lett. **272**, 127832 (2020).

[34] I. A. Ivanov, A. Ryskulov, A. Kurakhmedov, A. Kozlovskiy, D. Shlimas, M. V. Zdorovets, V. V. Uglov, S. V. Zlotski, and J. Ke, Radiation swelling and hardness of high-entropy alloys based on the titanbv system irradiated with krypton ions, J. Mater. Sci.: Mater. Electron. **32**, 27260 (2021).

[35] H. Gleiter, Nanocrystalline materials, Prog. Mater. Sci. **33**, 223 (1989).

[36] M. Meyers, A. Mishra, and D. Benson, Mechanical properties of nanocrystalline materials, Prog. Mater. Sci. **51**, 427 (2006).

[37] I. J. Beyerlein, A. Caro, M. J. Demkowicz, N. A. Mara, A. Misra, and B. P. Uberuaga, Radiation damage tolerant nanomaterials, Mater. Today **16**, 443 (2013).

[38] O. El-Atwani, J. E. Nathaniel, A. C. Leff, K. Hattar, and M. L. Taheri, Direct observation of sink-dependent defect evolution in nanocrystalline iron under irradiation, Sci. Rep. **7**, 1836 (2017).

[39] S. Zinkle and K. Farrell, Void swelling and defect cluster formation in reactor-irradiated copper, J. Nucl. Mater. **168**, 262 (1989).

[40] Y. Zhu, J. Luo, X. Guo, Y. Xiang, and S. J. Chapman, Role of grain boundaries under long-time radiation, Phys. Rev. Lett. **120**, 222501 (2018).

[41] O. El-Atwani, J. A. Hinks, G. Greaves, S. Gonderman, T. Qiu, M. Efe, and J. P. Allain, In-situ tem observation of the response of ultrafine- and nanocrystalline-grained tungsten to extreme irradiation environments, Sci. Rep. **4**, 4716 (2014).

[42] O. El-Atwani, J. A. Hinks, G. Greaves, J. P. Allain, and S. A. Maloy, Grain size threshold for enhanced irradiation resistance in nanocrystalline and ultrafine tungsten, Mater. Res. Lett. **5**, 343 (2017).

[43] G. Valles, M. Panizo-Laiz, C. González, I. Martin-Bragado, R. González-Arrabal, N. Gordillo, R. Iglesias, C. Guerrero, J. Perlado, and A. Rivera, Influence of grain boundaries on the radiation-induced defects and hydrogen in nanostructured and coarse-grained tungsten, Acta Mater. **122**, 277 (2017).

[44] Y. Wang, M. Chen, F. Zhou, and E. Ma, High tensile ductility in a nanostructured metal, Nature (London) **419**, 912 (2002).

[45] J. Schiøtz, F. D. Di Tolla, and K. W. Jacobsen, Softening of nanocrystalline metals at very small grain sizes, Nature (London) **391**, 561 (1998).

[46] O. El-Atwani, A. Suslova, T. Novakowski, K. Hattar, M. Efe, S. Harilal, and A. Hassanein, In-situ tem/heavy ion irradiation on ultrafine-and nanocrystalline-grained tungsten: Effect of 3 Mev Si, Cu and W ions, Mater. Charact. **99**, 68 (2015).

[47] O. El-Atwani, E. Esquivel, M. Efe, E. Aydogan, Y. Q. Wang, E. Martinez, and S. A. Maloy, Loop and void damage during heavy ion irradiation on nanocrystalline and coarse grained tungsten: Microstructure, effect of dpa rate, temperature, and grain size, Acta Mater. **149**, 206 (2018).

[48] O. El-Atwani, E. Esquivel, E. Aydogan, E. Martinez, J. K. Baldwin, M. Li, B. P. Uberuaga, and S. A. Maloy, Unprecedented irradiation resistance of nanocrystalline tungsten with equiaxed nanocrystalline grains to dislocation loop accumulation, Acta Mater. **165**, 118 (2019).

[49] M. Rose, A. Balogh, and H. Hahn, Instability of irradiation induced defects in nanostructured materials, Nucl. Instrum. Methods Phys. Res., B **127**, 119 (1997).

[50] S. Dey, J. W. Drazin, Y. Wang, J. A. Valdez, T. G. Holesinger, B. P. Uberuaga, and R. H. R. Castro, Radiation tolerance of nanocrystalline ceramics: Insights from yttria stabilized zirconia, Sci. Rep. **5**, 7746 (2015).

[51] M. Samaras, P. M. Derlet, H. Van Swygenhoven, and M. Victoria, Computer simulation of displacement cascades in nanocrystalline Ni, Phys. Rev. Lett. **88**, 125505 (2002).

[52] M. A. Tschopp, K. N. Solanki, F. Gao, X. Sun, M. A. Khaleel, and M. F. Horstemeyer, Probing grain boundary sink strength at the nanoscale: Energetics and length scales of vacancy and interstitial absorption by grain boundaries in α-Fe, Phys. Rev. B **85**, 064108 (2012).

[53] X.-M. Bai, A. F. Voter, R. G. Hoagland, M. Nastasi, and B. P. Uberuaga, Efficient annealing of radiation damage near grain boundaries via interstitial emission, Science **327**, 1631 (2010).

[54] X. Li, W. Liu, Y. Xu, C. Liu, B. Pan, Y. Liang, Q. Fang, J.-L. Chen, G.-N. Luo, G.-H. Lu, and Z. Wang, Radiation resistance of nano-crystalline iron: Coupling of the fundamental segregation process and the annihilation of interstitials and vacancies near the grain boundaries, Acta Mater. **109**, 115 (2016).

[55] M. Jin, P. Cao, S. Yip, and M. P. Short, Radiation damage reduction by grain-boundary biased defect migration in nanocrystalline Cu, Acta Mater. **155**, 410 (2018).

[56] M. Jin, P. Cao, and M. P. Short, Mechanisms of grain boundary migration and growth in nanocrystalline metals under irradiation, Scr. Mater. **163**, 66 (2019).

[57] D. Kaoumi, A. T. Motta, and R. C. Birtcher, A thermal spike model of grain growth under irradiation, J. Appl. Phys. **104**, 073525 (2008).

[58] P. Wang, D. A. Thompson, and W. W. Smeltzer, Implantation of Ni thin films and single crystals with Ag ions, Nucl. Instrum. Methods Phys. Res., B **7-8**, 97 (1985).

[59] P. Wang, D. A. Thompson, and W. W. Smeltzer, Implantation and grain growth in Ni thin films induced by Bi and Ag ions, Nucl. Instrum. Methods Phys. Res., B **16**, 288 (1986).

[60] D. C. Bufford, F. F. Abdeljawad, S. M. Foiles, and K. Hattar, Unraveling irradiation induced grain growth with in situ transmission electron microscopy and coordinated modeling, Appl. Phys. Lett. **107**, 191901 (2015).

[61] G. H. Vineyard, Thermal spikes and activated processes, Radiat. Eff. **29**, 245 (1976).

[62] E. Levo, F. Granberg, D. Utt, K. Albe, K. Nordlund, and F. Djurabekova, Radiation stability of nanocrystalline single-phase multicomponent alloys, J. Mater. Res. **34**, 854 (2019).

[63] F. Granberg, K. Nordlund, M. W. Ullah, K. Jin, C. Lu, H. Bei, L. M. Wang, F. Djurabekova, W. J. Weber, and Y. Zhang, Mechanism of radiation damage reduction in equiatomic multicomponent single phase alloys, Phys. Rev. Lett. **116**, 135504 (2016).

[64] F. Granberg, J. Byggmästar, and K. Nordlund, Molecular dynamics simulations of high-dose damage production and defect evolution in tungsten, J. Nucl. Mater. **556**, 153158 (2021).

[65] A. Chartier and M.-C. Marinica, Rearrangement of interstitial defects in alpha-Fe under extreme condition, Acta Mater. **180**, 141 (2019).

[66] P.-W. Ma, D. R. Mason, S. Van Boxel, and S. L. Dudarev, Athermal evolution of nanocrystalline tungsten driven by irradiation, J. Nucl. Mater. **586**, 154662 (2023).

[67] P. Hirel, Atomsk: A tool for manipulating and converting atomic data files, Comput. Phys. Commun. **197**, 212 (2015).

[68] M.-C. Marinica, L. Ventelon, M. R. Gilbert, L. Proville, S. L. Dudarev, J. Marian, G. Bencteux, and F. Willaime, Interatomic potentials for modelling radiation defects and dislocations in tungsten, J. Phys.: Condens. Matter **25**, 395502 (2013).

[69] C. H. Rycroft, VORO++: A three-dimensional Voronoi cell library in C++, Chaos **19**, 041111 (2009).

[70] J.-S. Ferenc and Z. Néda, On the size distribution of Poisson Voronoi cells, Physica A **385**, 518 (2007).

[71] D. R. Mason, D. Nguyen-Manh, and C. S. Becquart, An empirical potential for simulating vacancy clusters in tungsten, J. Phys.: Condens. Matter **29**, 505501 (2017).

[72] P. M. Derlet and H. Van Swygenhoven, Atomic positional disorder in fcc metal nanocrystalline grain boundaries, Phys. Rev. B **67**, 014202 (2003).

[73] S. Plimpton, Fast parallel algorithms for short-range molecular dynamics, J. Comput. Phys. **117**, 1 (1995).

[74] A. P. Thompson, H. M. Aktulga, R. Berger, D. S. Bolintineanu, W. M. Brown, P. S. Crozier, P. J. in 't Veld, A. Kohlmeyer, S. G.

Moore, T. D. Nguyen, R. Shan, M. J. Stevens, J. Tranchida, C. Trott, and S. J. Plimpton, LAMMPS - a flexible simulation tool for particle-based materials modeling at the atomic, meso, and continuum scales, Comput. Phys. Commun. **271**, 108171 (2022).

[75] M. Norgett, M. Robinson, and I. Torrens, A proposed method of calculating displacement dose rates, Nucl. Eng. Des. **33**, 50 (1975).

[76] J. Tian, H. Wang, Q. Feng, J. Zheng, X. Liu, and W. Zhou, Heavy radiation damage in alpha zirconium at cryogenic temperature: A computational study, J. Nucl. Mater. **555**, 153159 (2021).

[77] A. R. Warwick, R. Thomas, M. Boleininger, Ö. Koç, G. Zilahi, G. Ribárik, Z. Hegedues, U. Lienert, T. Ungar, C. Race, M. Preuss, P. Frankel, and S. L. Dudarev, Dislocation density transients and saturation in irradiated zirconium, Int. J. Plast. **164**, 103590 (2023).

[78] F. Ferroni, X. Yi, K. Arakawa, S. P. Fitzgerald, P. D. Edmondson, and S. G. Roberts, High temperature annealing of ion irradiated tungsten, Acta Mater. **90**, 380 (2015).

[79] K. Papamihail, K. Mergia, F. Ott, Y. Serruys, Th. Speliotis, G. Apostolopoulos, and S. Messoloras, Magnetic effects induced by self-ion irradiation of Fe films, Phys. Rev. B **93**, 100404(R) (2016).

[80] A. Stukowski, Visualization and analysis of atomistic simulation data with OVITO - the Open Visualization Tool, Modell. Simul. Mater. Sci. Eng. **18**, 015012 (2010).

[81] P. M. Larsen, S. Schmidt, and J. Schiøtz, Robust structural identification via polyhedral template matching, Modell. Simul. Mater. Sci. Eng. **24**, 055007 (2016).

[82] D. R. Mason, F. Granberg, M. Boleininger, T. Schwarz-Selinger, K. Nordlund, and S. L. Dudarev, Parameter-free quantitative simulation of high-dose microstructure and hydrogen retention in ion-irradiated tungsten, Phys. Rev. Mater. **5**, 095403 (2021).

[83] Y. Zhang, W. Jiang, C. Wang, F. Namavar, P. D. Edmondson, Z. Zhu, F. Gao, J. Lian, and W. J. Weber, Grain growth and phase stability of nanocrystalline cubic zirconia under ion irradiation, Phys. Rev. B **82**, 184105 (2010).

[84] W. Mohamed, B. Miller, D. Porter, and K. Murty, The role of grain size on neutron irradiation response of nanocrystalline copper, Materials **9**, 144 (2016).

[85] C. M. Barr, O. El-Atwani, D. Kaoumi, and K. Hattar, Interplay between grain boundaries and radiation damage, JOM **71**, 1233 (2019).

[86] S. L. Dudarev, Density functional theory models for radiation damage, Annu. Rev. Mater. Res. **43**, 35 (2013).

[87] D. L. Tonks, Percolation theory for the plastic yield transition, J. Appl. Phys. **65**, 105 (1989).

[88] H. Van Swygenhoven, D. Farkas, and A. Caro, Grain-boundary structures in polycrystalline metals at the nanoscale, Phys. Rev. B **62**, 831 (2000).

[89] A. P. Sutton and R. W. Balluffi, *Interfaces in Crystalline Materials* (Clarendon Press, Oxford, 1996).

[90] A. Stukowski, V. V. Bulatov, and A. Arsenlis, Automated identification and indexing of dislocations in crystal interfaces, Model. Simul. Mater. Sci. Eng. **20**, 085007 (2012).

[91] A. Bhattacharya and S. J. Zinkle, Cavity swelling in irradiated materials, in *Comprehensive Nuclear Materials*, 2nd ed., edited by R. J. Konings and R. E. Stoller (Elsevier, Amsterdam, 2020), Vol. 1, pp. 406–455.

[92] S. L. Dudarev and P.-W. Ma, Elastic fields, dipole tensors, and interaction between self-interstitial atom defects in bcc transition metals, Phys. Rev. Mater. **2**, 033602 (2018).

[93] M. Klimenkov, U. Jäntsch, M. Rieth, H. Schneider, D. Armstrong, J. Gibson, and S. Roberts, Effect of neutron irradiation on the microstructure of tungsten, Nucl. Mater. Energy **9**, 480 (2016).

[94] C. A. Hirst, F. Granberg, B. Kombaiah, P. Cao, S. Middlemas, R. S. Kemp, J. Li, K. Nordlund, and M. P. Short, Revealing hidden defects through stored energy measurements of radiation damage, Sci. Adv. **8**, eabn2733 (2022).

[95] J. S. Wróbel, M. R. Zemła, D. Nguyen-Manh, P. Olsson, L. Messina, C. Domain, T. Wejrzanowski, and S. L. Dudarev, Elastic dipole tensors and relaxation volumes of point defects in concentrated random magnetic Fe-Cr alloys, Comput. Mater. Sci. **194**, 110435 (2021).

[96] Please contact PublicationsManager@ukaea.uk.